nature portfolio

https://doi.org/10.1038/s41586-021-04296-3

Supplementary information

Irreversible synthesis of an ultrastrong two-dimensional polymeric material

In the format provided by the authors and unedited

Supplementary Materials for

Irreversible Synthesis of an Ultra-Strong Two-Dimensional Polymeric Material

Yuwen Zeng[1], Pavlo Gordiichuk[1], Takeo Ichihara[1], Ge Zhang[1], Sandoz-Rosado Emil[2], Eric D. Wetzel[2], Jason Tresback[3], Jing Yang[1], Daichi Kozawa[1], Zhongyue Yang[1], Matthias Kuehne[1], Michelle Quien[1], Zhe Yuan[1], Xun Gong[1], Guangwei He[1], Daniel Lundberg[1], Pingwei Liu[1], Albert Tianxiang Liu[1], Jingfan Yang[1], Heather J. Kulik[1], Michael S. Strano[1]*

[1]Department of Chemical Engineering, Massachusetts Institute of Technology, Cambridge, MA 02139, USA

[2]U.S. Army Research Laboratory, Aberdeen Proving Ground, MD 21005-5069, USA

[3]Center for Nanoscale Systems, Harvard University, Cambridge, MA 02139, USA

Table of Contents

Chemical Kinetic Modeling of 2D vs 3D Solution Polymerization

Homogeneous polymerization strongly disfavors the generation of 2D polymers, due to the unfavorable scaling of growth rate compared to 3D random polymers, and the lack of error correction.[1]

To elaborate on the scaling of growth rate, we may abstract this problem to consider monomers as structure-less beads of radius r_m and volume V_m. As the growth of the planar molecule comprised of i monomers (denoted as G_i) proceeds, the number of reactive sites along its periphery increases and hence so does the rate constant for addition. This is a fundamental difference compared to linear polymers. To determine this scaling, consider the radius and area of G_i as r_i and A_i respectively. The radius and area of the corresponding monomers are r_m and A_m respectively. Naturally,

$$r_i = \sqrt{\frac{A_i}{\pi}} \sim \sqrt{\frac{iA_m}{\pi}}$$

while the circumference is $2\pi r_i$. For large i, we can approximate the arc length occupied by a monomer as $2r_m$. Hence, the number of peripheral sites S_i available for addition on G_i grows as the square root of i:

$$S_i \approx \frac{2\pi r_i}{2r_m} = \frac{2\pi\sqrt{\frac{iA_m}{\pi}}}{2\sqrt{\frac{A_m}{\pi}}} = \pi\sqrt{i}$$

In terms of the rate constant for monomer addition per site, k_o, we expect the constant for the i+1 addition to be

$$k_i \approx k_o \pi\sqrt{i}$$

Meanwhile, the addition of a monomer to a 2D polymer G_{i-1} can also result in a defective 3D structure, which we label as D_i. The 3D random growth imparts a different rate constant scaling as we consider the volume and projected area V_m and A_m of the monomer, with corresponding V_{Di} and A_{Di} for the volume and surface area of D_i.

$$r_{Di} = \left(\frac{3V_{Di}}{4\pi}\right)^{\frac{1}{3}} \approx \left(\frac{3iV_m}{4\pi}\right)^{\frac{1}{3}}$$

Hence, the number of reaction sites S_{Di} on the surface of the growing sphere D_i scales as

$$S_{Di} \approx \frac{A_{Di}}{A_m} = \frac{4\pi r_{Di}^2}{\pi r_m^2} = \pi(i)^{\frac{2}{3}}$$

We then expect the rate constant for defective 3D random growth to scale as

$$k_{Di} \approx k_o \pi(i)^{\frac{2}{3}}$$

Given the discussion above, when all things being equal, the defect structure will grow faster with i to the 1/6 power (orange and blue solid straight lines, **Figure S1a**).

The geometric analysis of the number of reaction sites is supported by kinetic Monte Carlo (kMC) simulation results. As shown in **Figure S1a** (orange and blue dotted lines), the number of reactions sites for a 3D random polymer scales with $i^{0.73}$, which is faster than polymer confined to a 2D plane by $i^{0.16}$, consistent with the conclusion in the main text. The slight deviation from the ideal value is due to voids in the polymer that reduces its size, and the winding circumference leading to an increased perimeter length. **Figure S1b** shows that the addition of a monomer from a direction out of the polymer plane can prevent the planar ring closure reaction, thus leading to a permanent structure change from 2D to 3D.

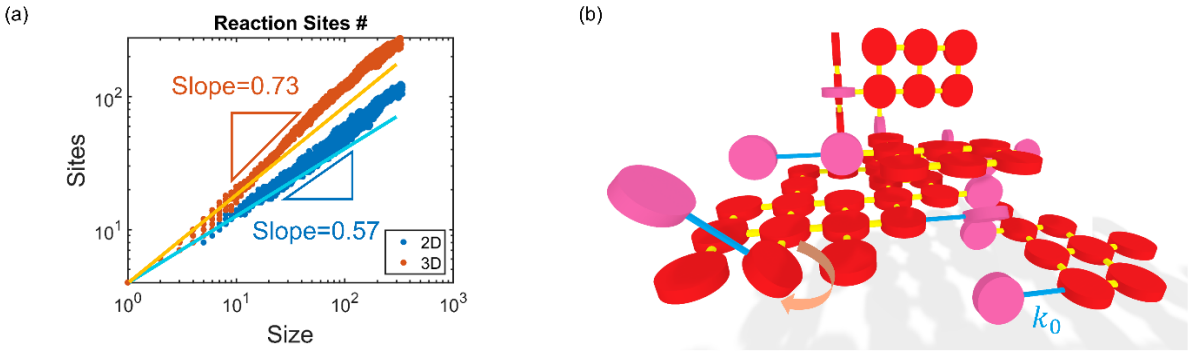

Figure S1. Schematics and scaling law. **a**, Reaction sites scaling with polymer size for 2D versus 3D polymer, blue solid lines are results from the theoretical scaling laws and dots are from kMC simulations. **b**, Schematics of 2D versus 3D growth, with out-of-plane bond formation illustrated by blue sticks, defective units are shown in pink rather than red.

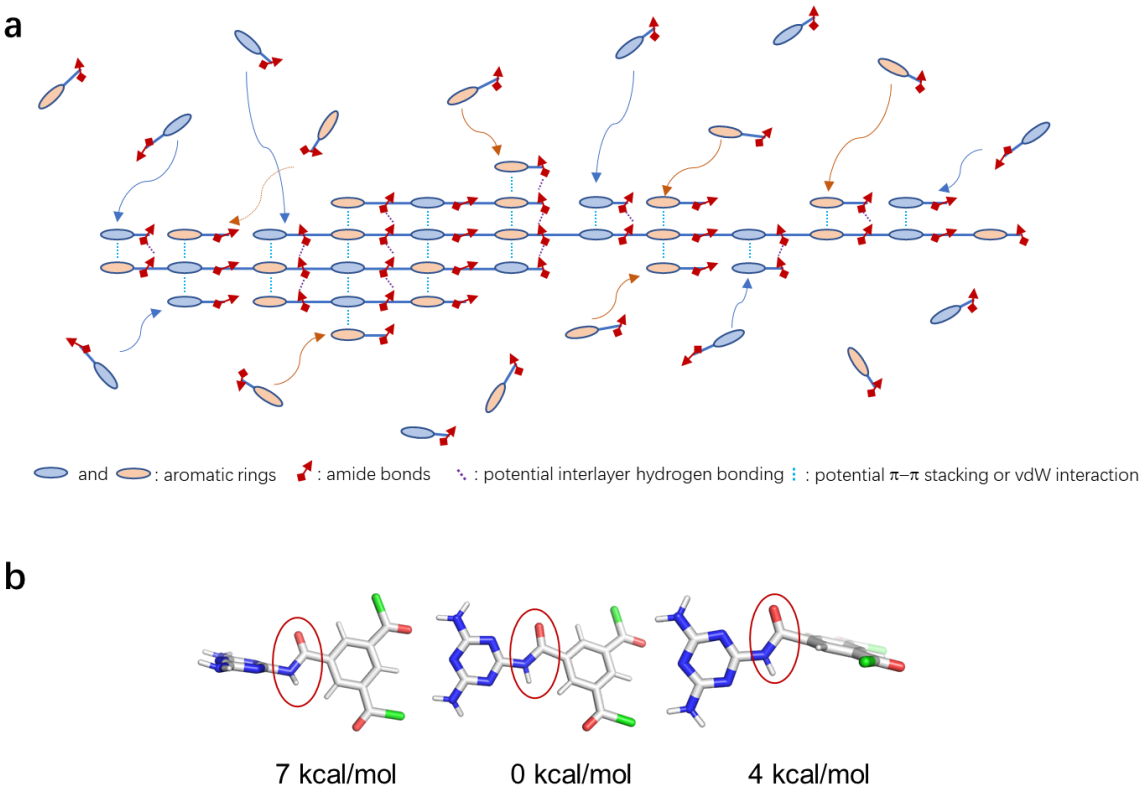

Figure S2. Schematic illustration of auto-catalysis by self-templating (**a**) and linkage in-plane tendency arising from linkage-core conjugations (**b**). Although both hydrogen bonding (nonspecific interlayer interaction) and π–π stacking (specific interlayer interaction) are included in **a** for simplicity, in real case they may act separately. Computational method used in **b**: Gas-phase geometry optimizations with Q-Chem v4.2 to compute 298 K conjugation enthalpies employed the ωB97-XD/6-311+G(d,p) DFT functional and basis set combination.

However, certain mechanisms could effectively suppress the defect formation and/or 3D growth. We have simulated two of these mechanisms, namely the autocatalysis and bond-planarity effects, characterized by two dimensionless parameters **β** and **γ** respectively (**Figure S2**). Where **β** represents a rate constant ratio of auto-catalyzed 2D growth pathway (**Figure S2a**) and non-catalyzed 2D growth pathway, and **γ** stands for an in-plane tendency of given linkages (**Figure S2b**), which equals to a probability ratio of in-plane and out-of-plane states. The reaction networks are shown below:

$$G_1 + G_{i-1} \xrightarrow{k_{i-1}} G_i$$

$$G_1 + G_{i-1} \xrightarrow{k_{i-1}/\gamma} D_i$$

$$G_1 + D_{i-1} \xrightarrow{k_{D,i-1}} D_i$$

$$G_1 + G_{i-1} + G_j \xrightarrow{\beta k_{i-1}} G_i + G_j$$

Here, G_1 is the monomer, G_i is the 2D polymer with i monomer units, D_i is the 3D polymer with i monomer units. The irreversible rate of addition is k_i and $k_{D,i}$ for 2D and 3D polymers respectively, where the former increases with $i^{1/2}$, and the latter increases with $i^{2/3}$. Parameter **γ** controls the rate of transformation from 2D to 3D defective polymer, and **β** dictates the rate ratio of auto-templated 2D growth and normal 2D growth.

In **Figure S3**, we show that both the average size and yield of 2D polymers are significantly enhanced as **β** and/or **γ** increases. The yield is above 90% even for moderate values of **β**=100 and **γ**=1000. Our calculations show for the first time from theory, the feasibility of producing two-dimensional polymers from irreversible polymerization in solution.

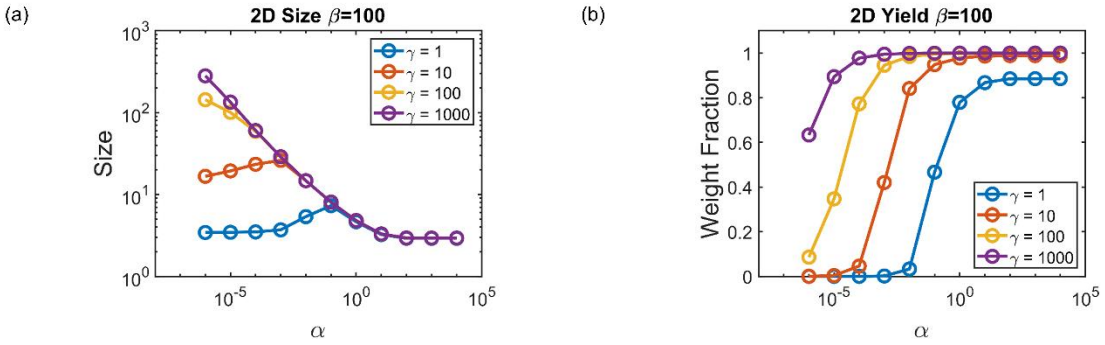

Figure S3. A combined effect of bond-planarity and autocatalysis. **a**, Average size of 2D polymers at different values of **γ** with **β** = 100. **b**, Yield of 2D polymers at different values of γ with **β** = 100. Parameter **α** describes the rate of monomer activation, which is not discussed here.

Note: This work has been recently published in *The Journal of Chemical Physics*, for more details, please see: *J Chem Phys* **2021,** *154* (19), 194901.

Synthesis and Characterization of 2DPA-1

Materials

Chemical reagents (melamine, trimesoyl chloride, $CaCl_2$, and pyridine) and anhydrous solvents (N-methyl-2-pyrrolidone, acetone, and trifluoroacetic acid) were purchased from *Aldrich* and used as received. For convenience, syntheses were conducted using standard Schlenk techniques or in an inert atmosphere glovebox unless otherwise stated. However, all starting materials can be also weighted and mixed in an ambient atmosphere and then sealed with a cape.

Thermal oxide wafers (SiO_2/Si, oxide thickness: 300 nm) were purchased from *Waferpro* and diced into certain sizes. TEM grids, highest grade V1 Mica discs, ultra-flat Si and SiO_2 substrates were obtained from *Ted Pella*. AFM probes (Arrow UHF, NPG-10, AC-160, and FASTSCAN-D-SS) were purchased from *Oxford Instruments*, *Bruker*, *Olympus*, and *NanoWorld*.

Polycarbonate (PC, granule) used in this research was purchase from *Aldrich* with an average molecular weight of 60K.

Characterization techniques

Thermogravimetric analysis (TGA) was operated on a *Discovery TGA-1* instrument under N_2 flow. Fourier-transform infrared (FTIR) measurements were performed by using a *Bruker* ATR-FTIR Spectrometer with a reflection diamond ATR module. Powder X-ray diffraction (PXRD) data was recorded on a *PANalytical X'Pert Pro* diffractometer using a Cu target (Kα1 radiation, λ = 1.54059 Å). Atomic force microscopy (AFM) images were collected using *Asylum MFP-3D*, *Asylum Cypher S*, and *Bruker Veeco Multimode 8* instruments and analyzed with *Gwyddion* or *Cypher*. Scanning electron microscopy (SEM) images were collected on a *Helios 660* from *FEI* and a *Sigma 300 VP* from *Zeiss*. Wide-angle X-ray scattering (WAXS) patterns were acquired on beamline 11-BM Complex Materials Scattering (CMS) of National Synchrotron Light Source II (NSLS-II) in the Brookhaven National Laboratory. N_2 sorption measurements were carried out on a Micromeritics ASAP 2020 System at 77K using a liquid N_2 bath.

Synthesis and Purification of 2DPA-1

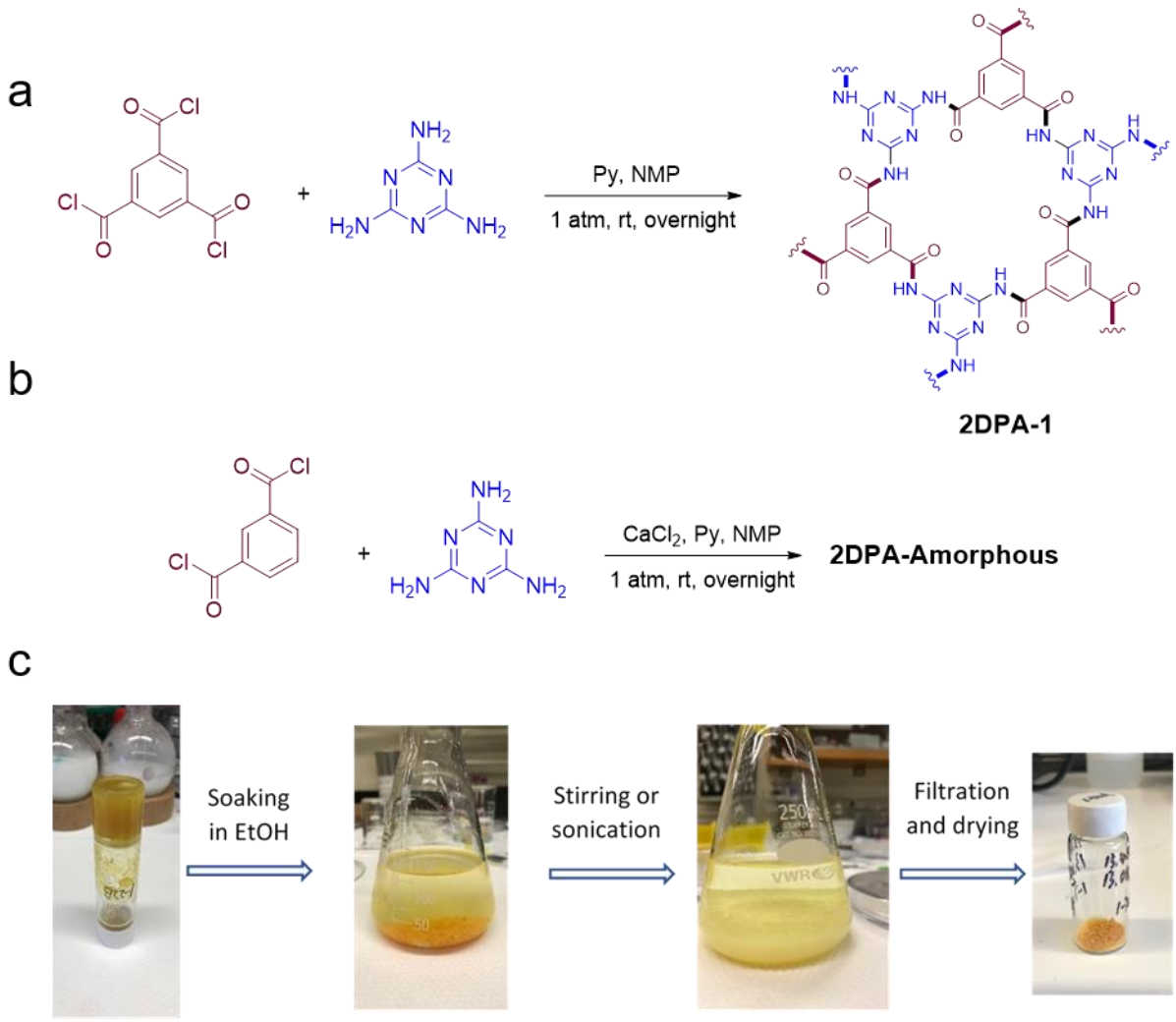

Figure S4. **a-b**, Synthetic scheme of **2DPA-1** and **2DPA-Amorphous**. **c**, Reaction work-up and purification of **2DPA-1.**

To a 40 ml glass vial equipped with a stir bar, trimesoyl chloride (265 mg, 1 mmol, 1 equiv) and melamine (126 mg, 1 mmol, 1 equiv) were added followed by anhydrous NMP (9 mL), and pyridine (1 mL). The reaction mixture was vigorously stirred overnight at room temperature. During the reaction course, the whole reaction system became a gel. This gel was cut into small pieces, mixed with 80 mL of ethanol, and stirred/sonicated to give a cloudy mixture. The resulting mixture was further filtrated or centrifuged, followed by H_2O (80 mL) and acetone (80 mL) washing. A pale-yellow powder was obtained after house-vacuum drying at 100°C for 8h.

Note: Although most of our synthesis was operated under N_2 atmosphere in a glovebox, it is just for convenience (most chemicals and anhydrous solvents were stored in glovebox), not mandatory. Starting

materials are stable enough to weigh in air and the 2D condensation is not sensitive to O_2. We observed no difference when the reaction is carried out in air and sealed with a cap.

2DPA-Amorphous is synthesized when trimesoyl chloride (1 equiv) is replaced by isothaloyl chloride (1.5 equiv) under standard conditions and the same purification method was used (**Figure S6**). **2DPA - Amorphous** serves as an amorphous control in this study.

Chemical stability and solubility of 2DPA-1 in strong acid

It is well known that most 2D materials made from reversible chemistries (2D COFs for example) possess low chemical stabilities, especially towards strong acids.[1,2] However, in organic chemistry, amide bonds are considered as stable chemical bonds under ambient conditions[3] (rate constant for hydrolysis are of the order of 10^{-11} s^{-1}), as well as in acidic and basic aqueous solutions.[4] Moreover, polyaramid such as *p*-phenylene terephthalamide (PPTA, also known as Kevlar) can stand in 100% of sulfuric acid at 80^{o}C for at least 30 min during the wet-spinning process.[5]

During our investigation, we made several **2DPA-1** stock solutions (2-5 mg/mL in trifluoroacetic acid, TFA). No oxygen or water-free operation is needed though caps with PTFE lining are used to prevent the solvent vapor from escaping. We observed no significant degradation over a long period (> 3 months) during our HR-AFM and spin-coated film studies.

2DPA-1 is insoluble in water and common organic solvents; however, it dissolves quickly in TFA to form a clear, pale-yellow solution. No residue is observed in this solution. Dark-field dynamic light scattering study[6] was performed and its result indicated that there are no particles larger than 30 nm (detect limit) in a 1 mg/mL solution. Given that the molecular size of **2DPA-1** is around 10 nm, we conclude that there are no molecular aggregations but only single molecules in the solution.

Mechanical stability of 2DPA-1

2DPA-1 is stable to bath sonication, which is often used for reaction work up, purification, and dispersion. No obvious adverse effects were observed.

Thermogravimetric Analysis (TGA)

Method: Few milligrams of samples were placed in a high-temperature Pt pan and mounted on a *Discovery TGA-1* instrument. The measurement was done under N_2 flow with a ramp rate of 5 degrees per minute.

2DPA-1 shows a sharp decomposition curve starting at 312°C, corresponding to 5% weight loss. A direct comparison between melamine, **2DPA-Am**, and **2DPA-1** TGA curves and their first derivatives (DTG curves) are also shown in **Figure S5**.

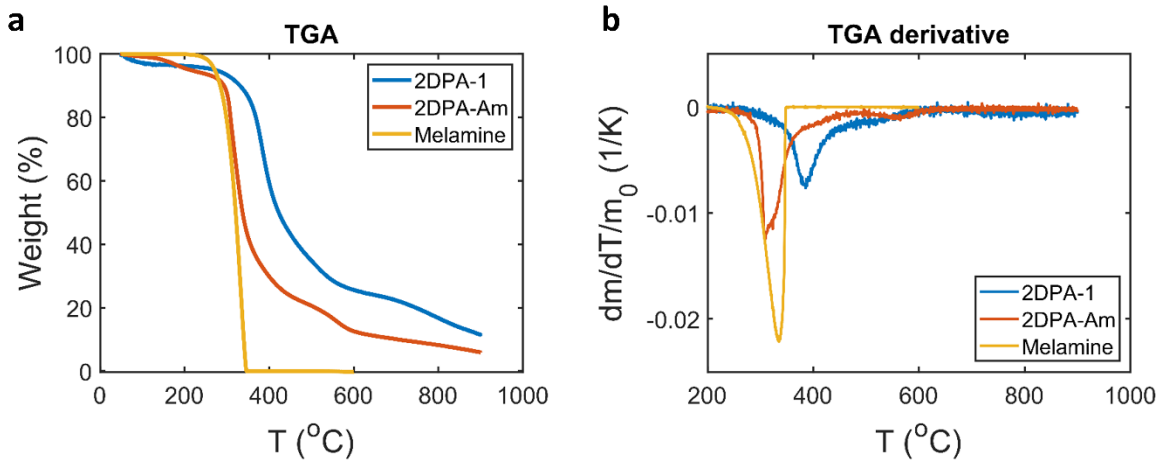

Figure S5. Thermogravimetric analysis (TGA) curves of melamine, **2DPA-Am** and **2DPA-1** (**a**) and their derivative thermogravimetry (DTG) curves (**b**). Samples were measured under N_2 flow. Ramp rate: 5°C /min to 900°C; isothermal at 50°C for 1 min.

Purity estimation: The purity (weight fraction) of crystalline 2D polymer in the reaction product could also be estimated from the thermogravimetric analysis (TGA) data. We assume that the **2DPA-1**sample contains both crystalline 2D polymer and amorphous 3D polymer, where the 2D one is the desirable "pure" product. We can then approximate the TGA behavior of amorphous 3D polymer with that of the sample **2DPA-Am**. The TGA curve of a pure crystalline 2D polymer can be calculated by subtracting the contribution of amorphous 3D polymer from the whole TGA curve of **2DPA-1**, providing we already know the purity. An upper bound of amorphous weight fraction (denoted as x) can be drawn, as the weight change ($\frac{dm}{dT}$) should be negative for both types of 2D polymers. Therefore, we can derive the following equation:

$$(1-x)\frac{d}{dT}m_{\text{2DPA-Cry}} = \frac{d}{dT}m_{\text{2DPA-2}} - x\frac{d}{dT}m_{\text{2DPA-Am}} < 0$$

The differential weight change curves of crystalline 2D polymer, with different assumptions of amorphous weight fractions (x) are shown in **Figure S6**. The weight fraction of amorphous impurity should be bounded by 5%, otherwise the weight change ($\frac{dm}{dT}$) would be positive as depicted below. This analysis indicates a very high 2D percentage exceeding 95%.

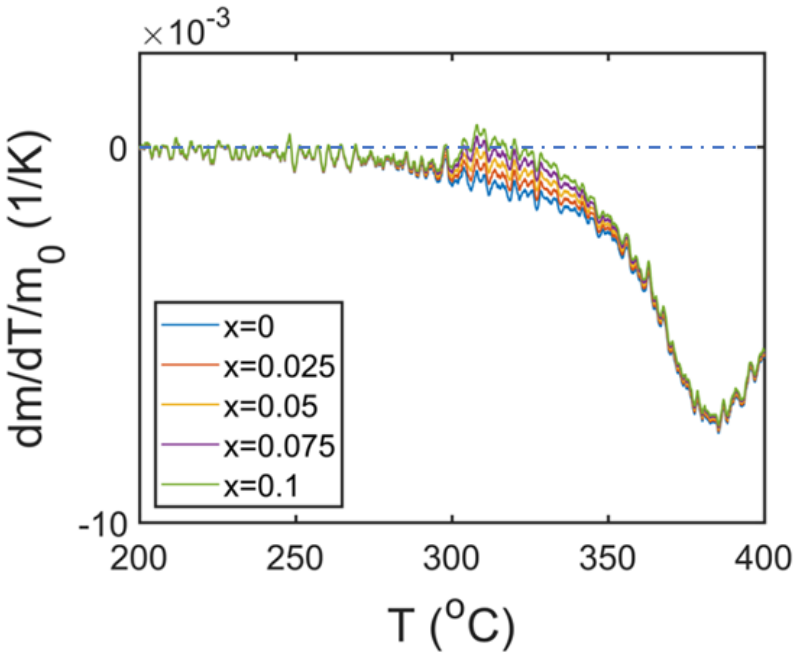

Figure S6. Differential thermogravimetric curves of pure crystalline 2D polymer derived using the above equation with different assumptions of amorphous weight fraction x.

Thermal stability of 2DPA-1 nanofilms: We found that suspended nanofilms are stable at 300°C for at least 1min without any obvious damage be observed.

Fourier-Transform Infrared (FT-IR) Spectroscopy

All FT-IR spectra were collected on a *Bruker* ATR-FTIR Spectrometer with a reflection diamond ATR module. The FT-IR spectrum of **2DPA-1** clearly indicates that all starting materials were entirely consumed or removed after reactions.

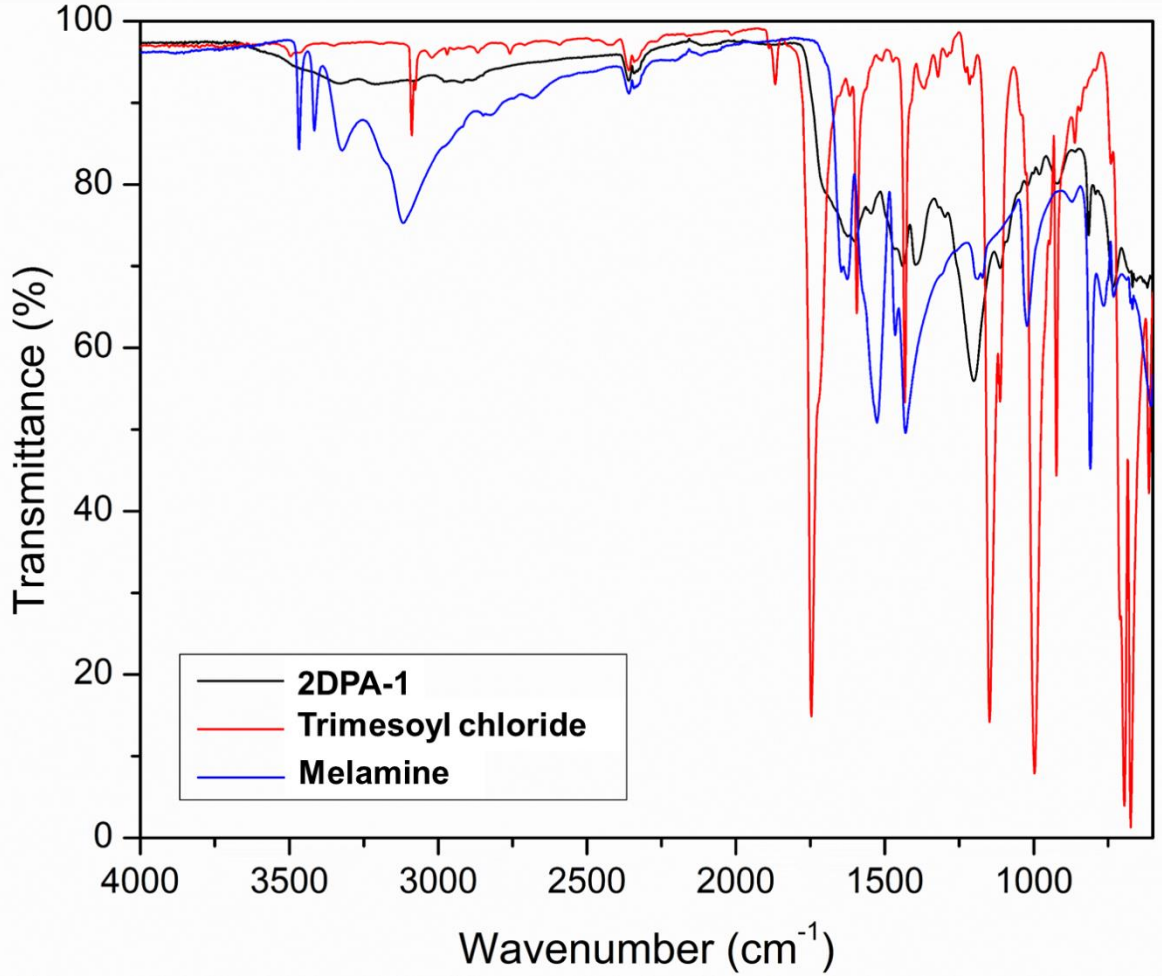

Figure S7. FT-IR spectra of **2DPA-1** (black), trimesoyl chloride (red), and Melamine (blue)

Figure S8 confirms the formation of the amide linkages in both amide **I** (1600-1700 cm^{-1}) and amide **II** (1500-1600 cm^{-1}) regions.[7] The broadened peaks suggest that the amides exist in heterogeneous chemical environments. Multiple broad and red-shifted peaks between 2800 and 3500 cm^{-1} are assigned to highly hydrogen-bonded N-H stretching.[8] This observation suggests that the condensed material contains amides that tilt out of the plane, forming interlayer hydrogen bonds.[9]

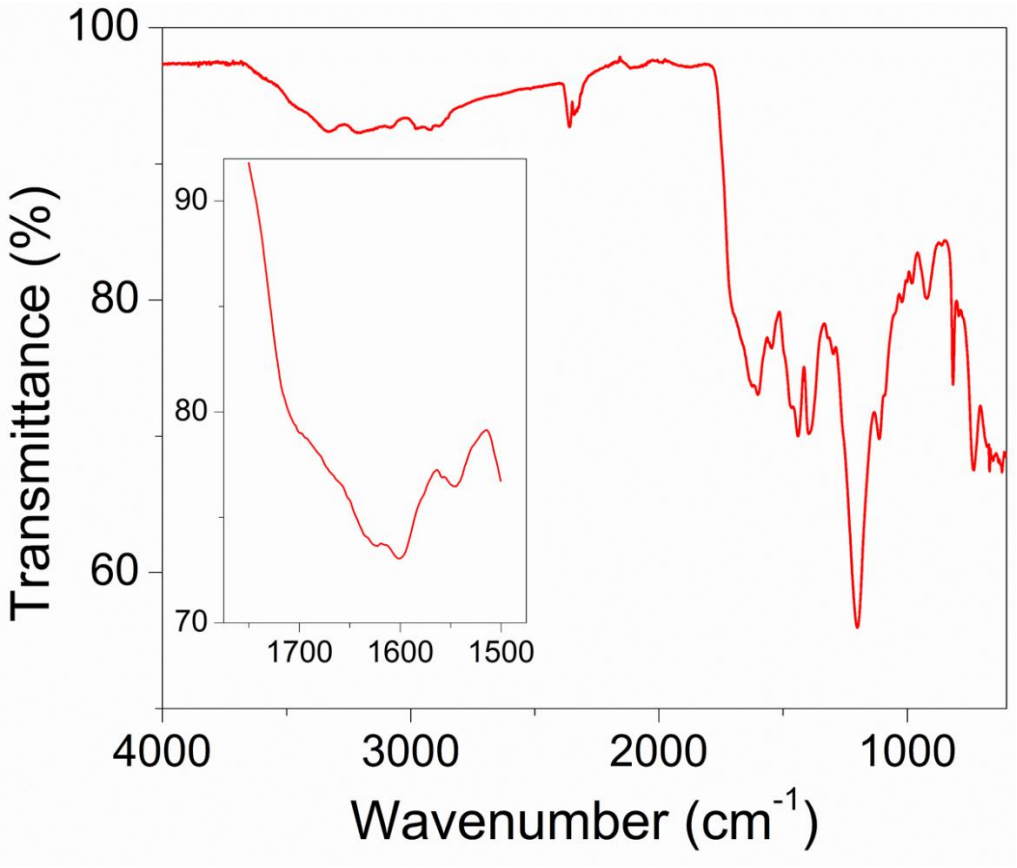

Figure S8. The whole FT-IR spectrum of **2DPA-1** and its amide region is shown in the inset.

Powder X-ray Diffraction (PXRD)

Characterization detail: The as-synthesized **2DPA-1** powder was grounded and placed onto a spinning zero-background Si substrate. PXRD measurement was then performed on a *PANalytical X'Pert Pro* instrument using a Cu target (Kα1 radiation, λ = 1.54059 Å). Sample stage: Open Eularian Cradle (OEC); Temperature: 25°C; 2 Theta range: 5-60 degree.

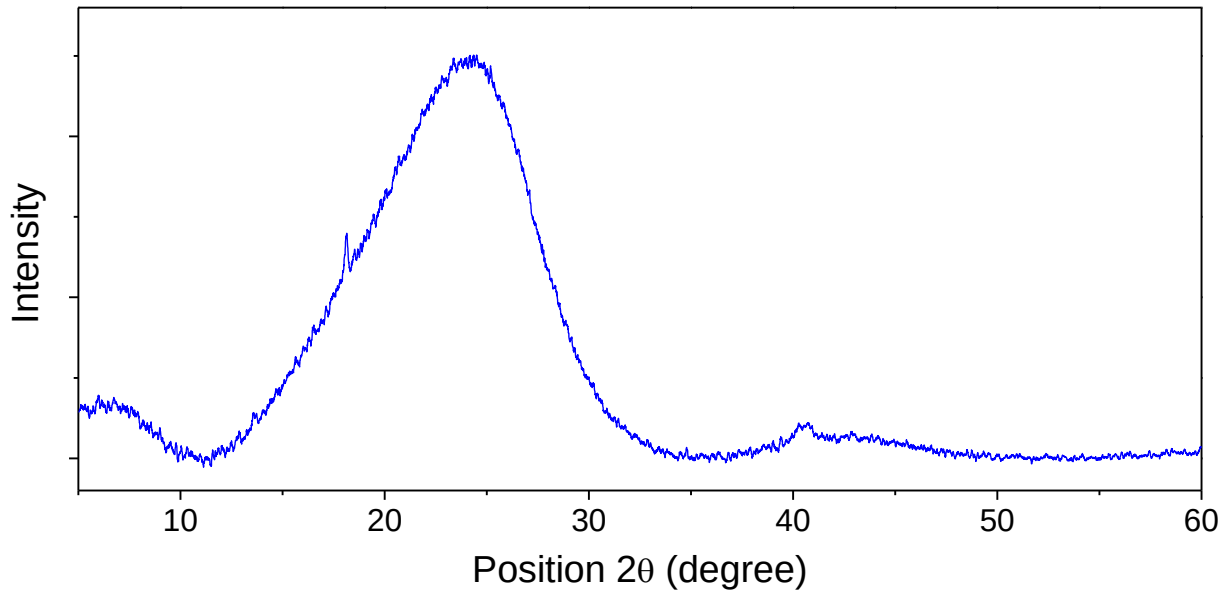

Figure S9. Powder X-ray diffraction (PXRD) of **2DPA-1** powder

The main peak centered at 24.3 degrees corresponds to an average interlayer spacing of 3.66 Å, which agrees with the spacing from GIWAXS (3.72 Å, discussed later in SI).

According to the Scherrer equation, the mean size of crystal domains can be determined by the line broadening at half the maximum intensity (FWHM).[10]

$$\tau = \frac{K\lambda}{\beta cos\theta}$$

Where τ is the mean size of ordered domains (lateral size of individual 2D molecules); K is the dimensionless shape factor, has a typical value of about 0.9; λ is the X-ray wavelength; β is the line broadening (FWHM), in radians; and θ is the Bragg angle.

the calculated mean ordered domain size τ is 18.3 Å, corresponding to a few layers (4-8) in primary particles in as-synthesized powders. It should be noted that this length is about 1/5 of that of the typical COF (considering an FWHM of 1.5-2 degrees for 001 peak). The imperfect crystallinity is also in line with our AFM observations (**Figure S19**), which support staggered and interlocked layered stacking.

The broad peak at 24.3 degrees (001 peak) in PXRD also has a second component, increasing the broadening further still. As shown later in the GIWAXS data, we find an amorphous ring at about 0.17 $Å^{-1}$ away from the stacking arc. This amorphous feature should also exist and contribute to the PXRD data, resulting in peak asymmetry and anisotropic broadening of the 001 peak.

BET surface area measurement

The BET surface area is measured by using a Micromeritics ASAP 2020 automatic gas sorption analyzer, and then calculated from N_2 sorption isotherm at 77K over the pressure range 0.01-0.20 P/P_0.

As-synthesized **2DPA-1** samples (two different batches) were measured after being dried at different temperatures (80, 150, 250 ^oC) and none of them gave meaningful BET surface area numbers (< 10 m^2/g, beyond the limit of instrument). This observation (**Table S1**) clearly indicates that the bulk materials do not have accessible free volume or internal surface, which agrees well with our bulge test mentioned above. Also note that drying at high temperatures does not help with the BET surface area, implying pores are not clogged by small residual solvent molecules. The consistently low BET surface area of <10 m^2/g and the impermeability of cast films of **2DPA-1** indicate that stacking does not align the pores or rings within the molecule. Intermolecular gaps between molecular platelets must be small due to the negligible free volume for gas permeability but stacking mis-alignment in plane is also possible.

Table S1. Surface area of **2DPA-1** for different batches and drying conditions.

Sample info	Drying conditions	BET surface area
Batch 1	80 ^oC	4.45 m^2/g
Batch 2	80 ^oC	10.0 m^2/g
Batch 2	150 ^oC	0.68 m^2/g
Batch 2	250 ^oC	0.46 m^2/g

Transmission Electron Microscopy (TEM) Characterization

Preparation of TEM samples: The as-synthesized **2DPA-1** powder was mixed with MeOH (0.1 mg in 1 mL) and sonicated for 1 min. The dilute mixture was then drop-casted onto a lacey carbon/Cu TEM grid. TEM characterization was conducted after drying.

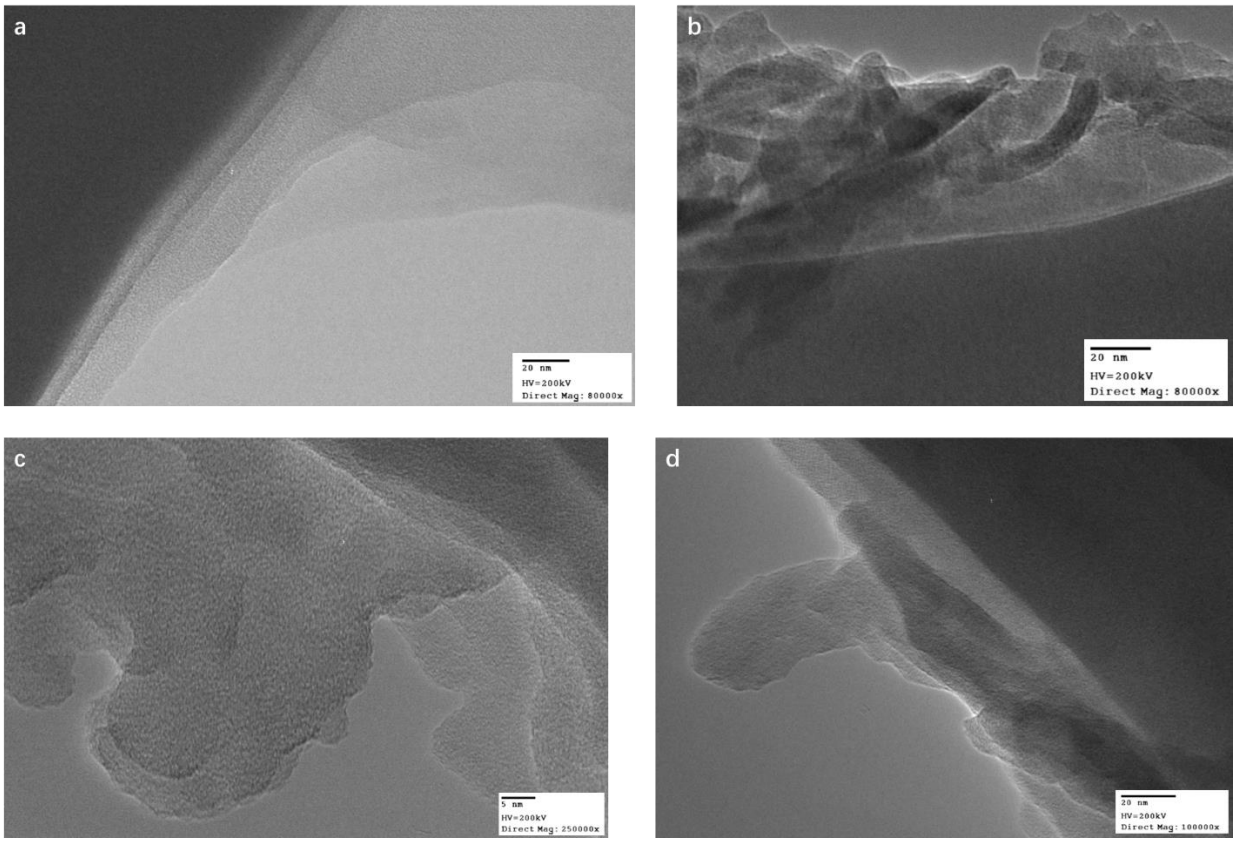

Figure S10. Transmission Electron Microscopy (TEM) images of layered structures at the edge of liquid exfoliated **2DPA-1** powder

Terrace nanostructures were observed at the edge of liquid exfoliated powders, although the thickness of each step is unknown.

High-Resolution Atomic Force Microscopy (AFM) Characterization

Method: Images were collected using a *Cypher S* (Asylum Research Oxford Instruments) AFM, or a *Veeco Multimode 8* (Bruker) AFM in AC mode. Data was analyzed with *Gwyddion* or *Asylum* AR*14* (Cypher's built-in analysis module). Ultra-high frequency proves (*Arrow UHF*) or Bruker FASTSCAN-D-ss probes were used under blue drive mode with a small laser.

Controlled experiment: A freshly cleaved mica was measured (**Figure S11**) and showed an ultra-flat surface with an RMS roughness less than 40 pm over a 5*5 um area (normally 20-40 pm, calculated from *Asylum AR14*).

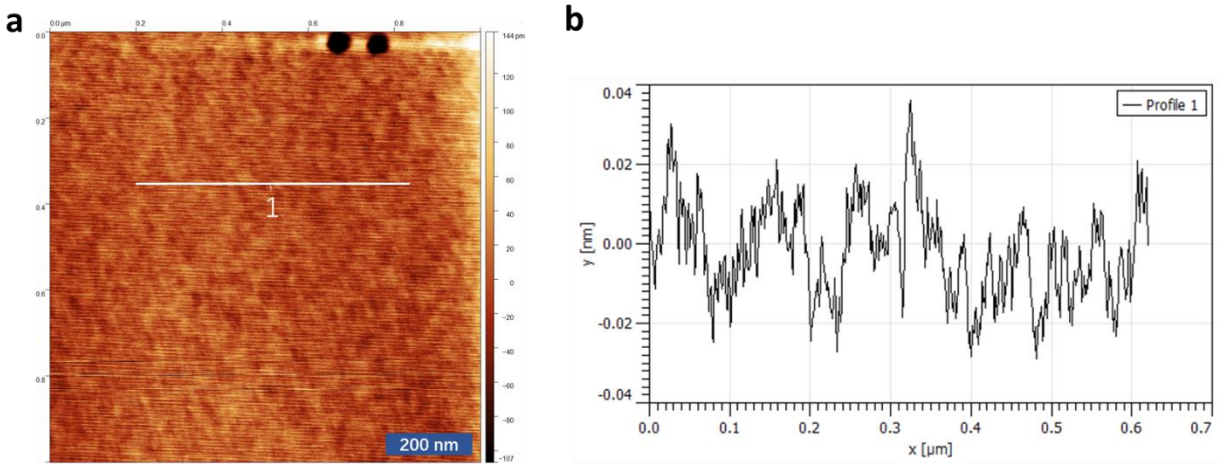

Figure S11. AFM topologic image of a freshly cleaved mica surface (**a**) and its height profile along the white line (**b**).

***Sample preparation*:** Mica is freshly cleaved and used immediately as an ultra-flat substrate. **2DPA-1** powder was dissolved in TFA (0.01 mg/mL) and spin-coated (2000 rpm) onto a mica substrate. The sample was then immersed in water several times and scanned with an *Asylum Cypher S* AFM in AC mode.

Note: Samples are prepared in situ and examined immediately. Contaminations (presumably hydrocarbons) and sample changes (creeping of molecules) are observed even after few hours.

Due to the strong intermolecular interaction, even at very low concentrations, single molecules tend to pair with other single molecules rather than sit on the bare mica surface, leading to the formation of bilayer clusters. Indeed, for **2DPA-1**, we never saw discrete individual molecules but bilayer aggregates. However, it is possible that sometimes single molecules are partially laying on other molecules, give terraces at the bilayer edges.

Data from 2DPA-1

One single molecule (part of it lay on other molecules) is measured and shown in **Figure S12**. Its height is measured at three different places. The mean values of the mica and platelet surfaces are determined by *Gwyddion*, using zero-order polynomial fitting.

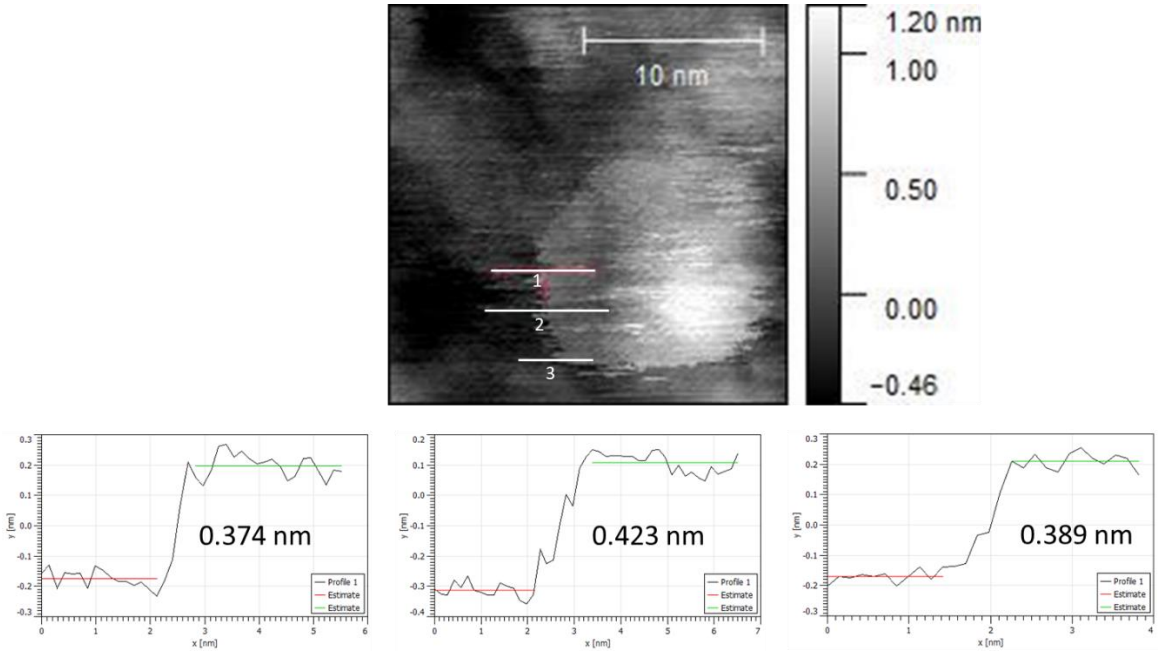

Figure S12. High-resolution atomic force microscopy (HR-AFM) image of one individual molecule absorbed on mica surface (top) and its height profiles along white lines (bottom). Both red and green lines in height profile images are fitted by *Gwyddion*, using zero-order polynomial functions (averaging of the curves).

For this particular single molecule, its mean height and the standard deviation is 3.95±0.20 Å. More monolayers were picked out from other images with slightly lower resolutions (due to bigger tip radius, measured with UHF Arrow probes, tip radius around 8 nm) and listed below (**Figure S13**). From these eight platelets, a mean thickness is obtained as 4.04±0.48 Å. Meanwhile, the mean thickness of bilayer clusters is 7.95±0.72 Å (**Figure S14**).

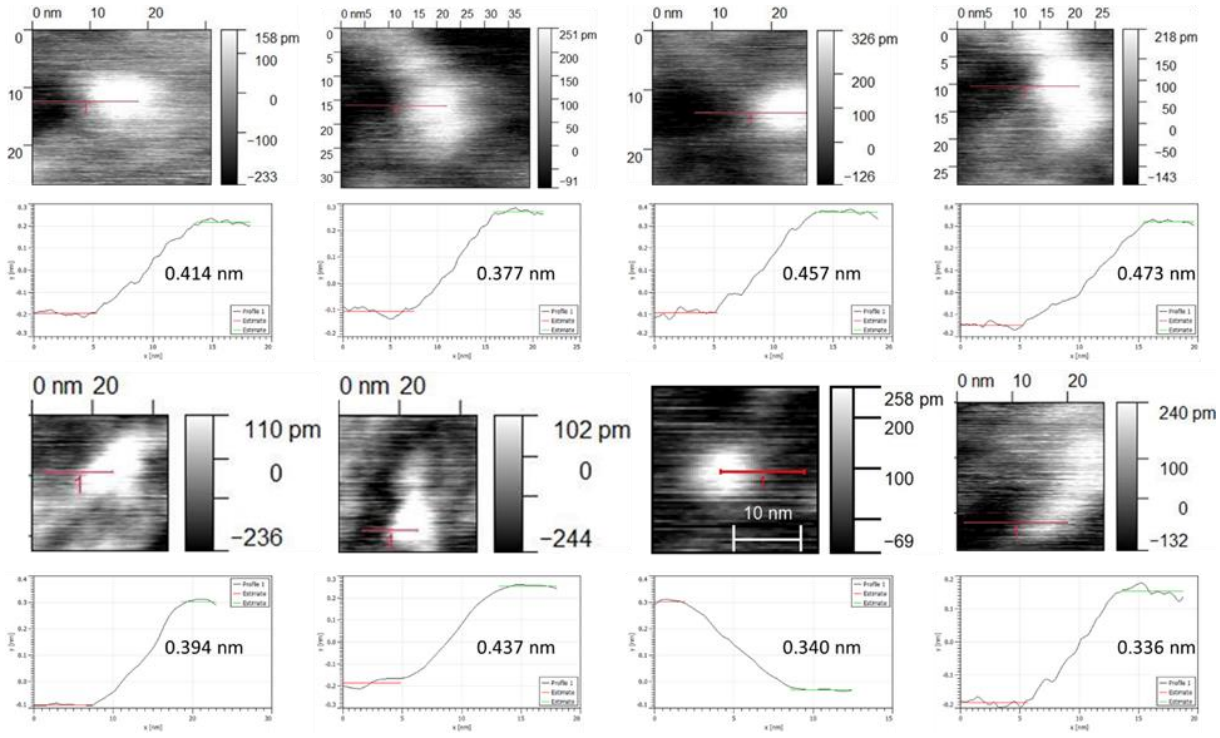

Figure S13. Monolayers and their thicknesses. The monolayers are chosen nearby bare mica surface to offer a flat background.

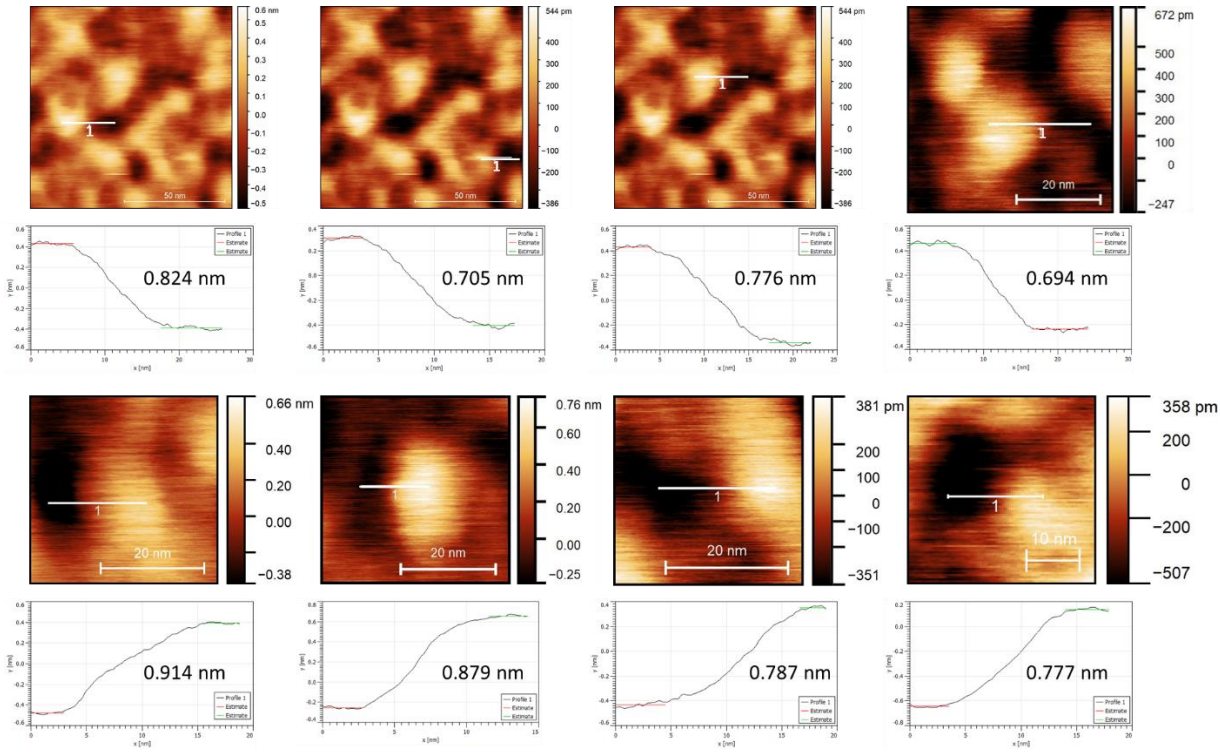

Figure S14. Bilayer clusters and their thicknesses.

Data from TMS-2DPA-1

Although the data shown above yield terrace structures of monolayers and bilayers, these terraces do not produce high quality images as they are necessarily obtained at the edge of bilayers or larger clusters, rather than discrete individual molecules and bilayers. To get more precise images of the molecular thickness, one needs to disperse the single molecules discretely on a flat substrate of low rms roughness, which we observe to be difficult for **2DPA-1** presumably due to its strong aggregation tendency. To shut down the strong intermolecular hydrogen bonding and break bilayers apart, we developed a highly reactive electrophile (TMSOTf) for post-modification (**Figure S15**). The consuming of amides is evidenced by the dissolution of **2DPA-1** in $CHCl_3$ and the disappearance of amide peaks after reaction. This chemical modification should allow a high ratio of individual **TMS-2DPA-1** molecules for AFM characterization while keep original molecular shapes. Although the changing in molecular height depends on the angle of amide bonds and its overall silylation conversion, the **TMS-2DPA-1** should not change its thickness dramatically but keep its monomer-like-thickness.

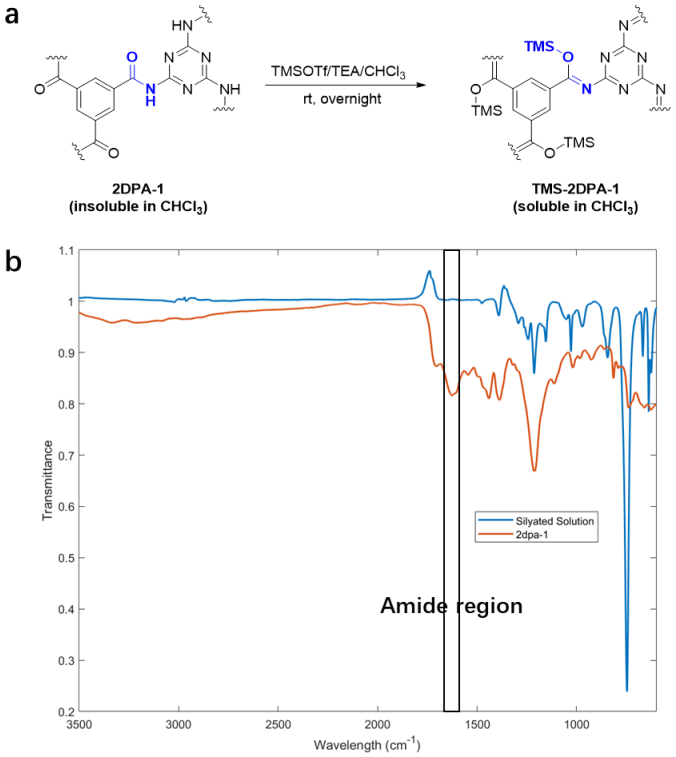

Figure S15. Synthetic scheme (**a**) and FT-IR (**b**) of **2DPA-1** silylation.

Indeed, **TMS-2DPA-1** has a high individual molecule ratio (**Figure S16, left**) and constant heights (**Figure S16, right**). Molecules are circular or oval, and its mean thickness is 3.69±0.28 Å (from 16 molecules), similar to that of conventional monolayer 2D materials such as graphene and hBN, undoubtedly prove its 2D nature.

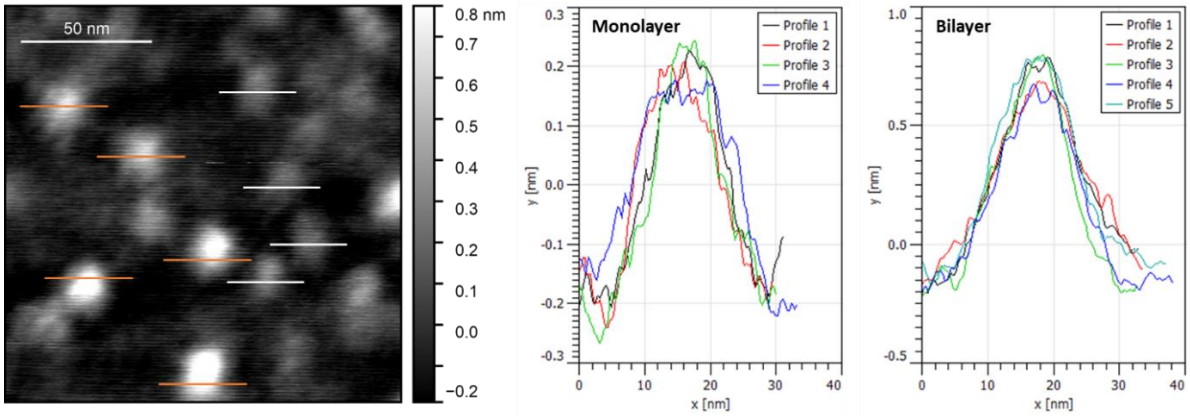

Figure S16. AFM characterization of **TMS-2DPA-1** on freshly cleaved mica. Height profiles were obtained along the white lines (individual molecules) and orange lines (bilayer platelets).

The mean diameter normalized by area is found to be 10.3±2.8 nm. Both the size distributions of monolayers and bilayers are shown below (**Figure S17, a&b**). It is worth noting that the bilayer distribution well agrees with the platelet size distribution obtained from a **2DPA-1** film surface (**Figure S17, c&d**), supporting our hypothesis that films are composed of bilayers.

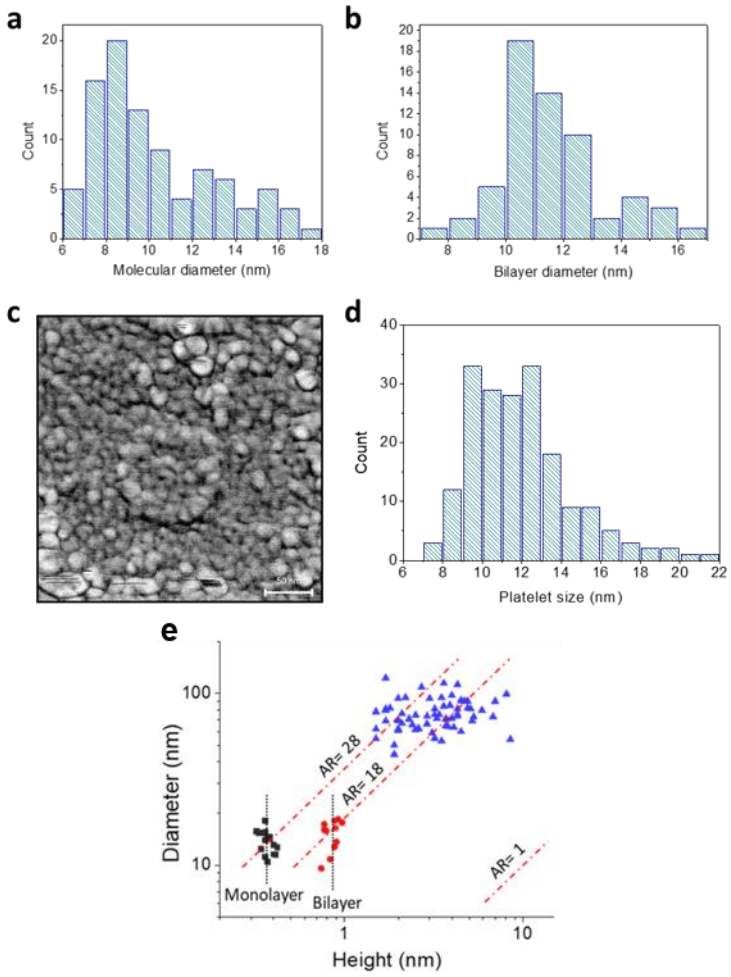

Figure S17. **a**, Size distribution of single **TMS-2DPA-1** molecules. **b**, Size distribution of bilayers from **TMS-2DPA-1**. **c**, Amplitude topology obtained at the second eigenmodes from a **2DPA-1** film surface. Scale bar: 50 nm. **d**, Platelet size distribution from the **2DPA-1** film surface. **e**, Plot of diameter against height for monolayers (black squares) and bilayers (red dots) from **TMS-2DPA-1**, as well as **2DPA-Am** (blue triangles, amorphous counterpart of **2DPA-1**, obtained when trimesoyl chloride is replaced by isophthaloyl chloride under standard conditions). Red dotted lines represent shapes at constant aspect ratio AR.

Defect quantifying of 2DPA-1

The acyl residue-to-monomer ratio (A/M) can be measured by ^{1}H NMR after IPA quenching (**Figure S18**). This A/M ratio consists of two parts: unreacted acyl groups at periphery and defects in the lattice. The edge acyl residues are inevitable and have a lower limit when the molecule has a perfect hexagonal lattice, while an upper limit of defect density can be obtained by subtracting the edge contribution from the experimental A/M ratio. The A/M ratio for a perfect hexagonal lattice (no interior defect) is inversely proportional to its molecular radius. However, this ratio increases quickly when the edge is branched, or some monomers are removed from the interior of lattice.

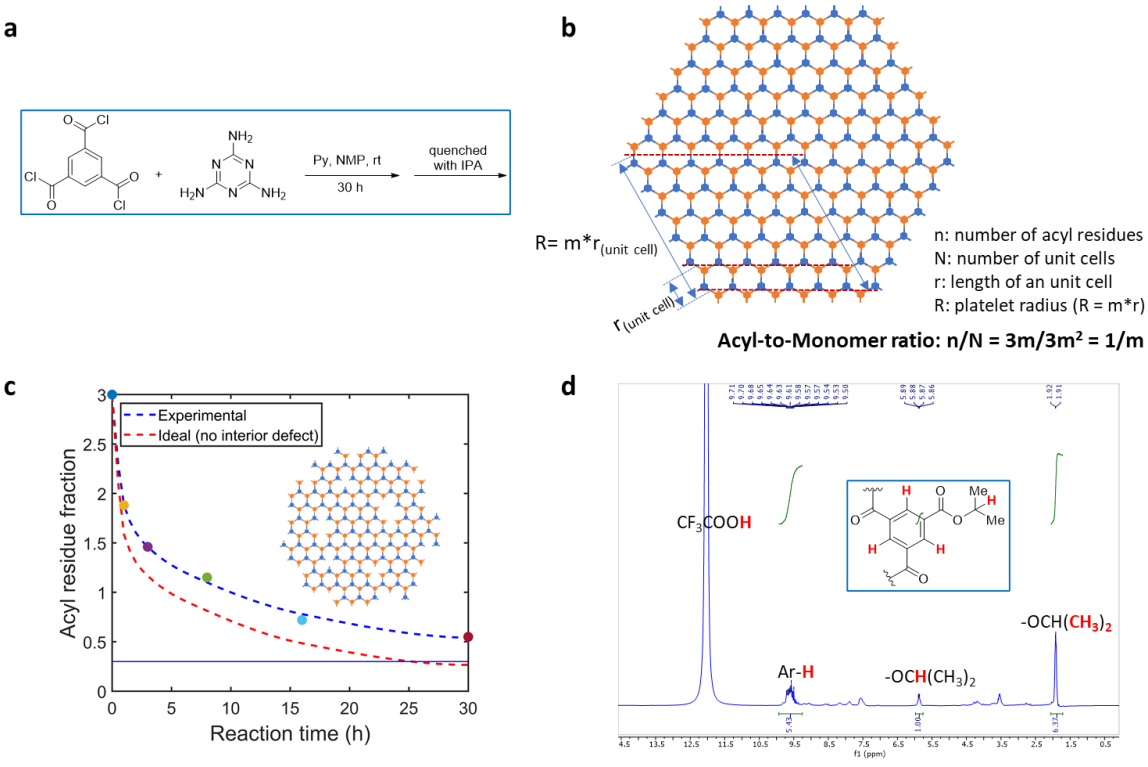

Figure S18. **a**, Acyl residue quenching after synthesis. **b**, Acyl-to-monomer (A/M) ratio for a perfect hexagonal lattice and its calculation. **c**, NMR characterization for defect-to-monomer ratio calculation. **d**, NMR spectrum at 30h.

We found that after 30h of reaction, an A/M ratio of 0.55 is observed (**Figure S18c**). For 2D molecules with a mean diameter of 10 nm, the acyl fraction from periphery would be no less than 0.25 (when the molecule has a perfect hexagonal shape), corresponding to an interior defect contribution of no more than 0.30. This ratio is translated to an interior defect density of 0.286 acyl/nm^2. It would be noted that as real molecules are all branched, its real interior defect density would be much smaller than the idea case. So, actual **2DPA-1** molecules would resemble the structure in **Figure S18c**, and its porous lattice may stem from condensation of small 2D fragments.

Film Characterization

***Preparation of 2DPA-1 thin films*: 2DPA-1** powder was allowed to dissolve in different amounts of trifluoroacetic acid (TFA), forming clear homogenous solutions. Spin-coating of those solutions onto clean SiO_2/Si wafers offers flat and uniform thin films.

Note: To get uniform thin films on SiO_2/Si wafers, substrates have to be pre-cleaned with acetone and isopropanol using a bath sonicator. Dust and contaminations will lead to imperfection and discontinuity.

Film thickness measurement: Prepare **2DPA-1** solutions with different concentrations (0.5, 1, 2, 5, 10, and 15 mg/mL in TFA). Prepare thin films by spin-coating (2000 rpm, 1 min) onto square substrates (length around 1.5 cm). Each concentration was repeated four times. Make scratches with a fine needle and then measure the film thickness using an AFM at scratches (**Figure S19**). Each sample was measured at five different places to get statistics (**Figure S20**). A nice correlation of film thickness and solution concentration is observed (**Figure S21**). Alternatively, the film thickness can be also measured by TEM and SEM. In most cases, AFM is used as it is handy and facile.

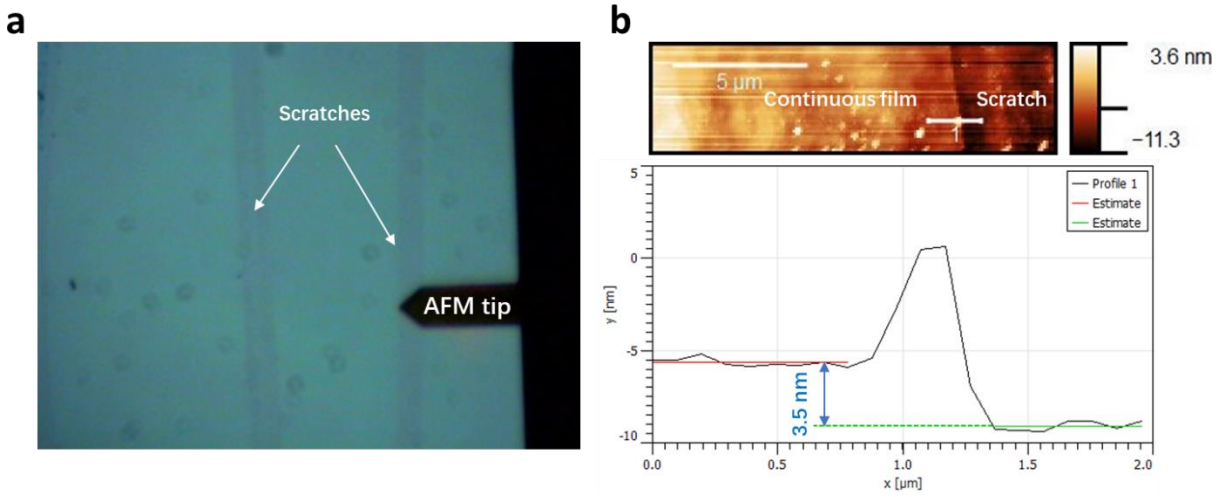

Figure S19. **a,** Optical micrograph of thickness measurement. Black dots are dirt on the optical lens. Scratches were made with a fine needle. **b,** Topological image of a thin-film and its thickness profile along the white line. White dots on the thin-film are residual materials made by scratching.

Concentration: 15 mg/mL				
	Sample			
	A	B	C	D
Place 1	139	119	136	115
Place 2	152	107	118	112
Place 3	147	91	148	150
Place 4	100	144	127	148
Place 5	109	167	80	103
Average	129.4	125.6	121.8	125.6
Error	20.94373	26.97851	23.13785	19.52025
Average (Total)	125.6			
Error (Total)	22.97694497			

Concentration: 10 mg/mL				
	Sample			
	A	B	C	D
Place 1	80	87	70	80
Place 2	82	84	77	79
Place 3	78	85	87	78
Place 4	86	84	84	75
Place 5	72	81	79	66
Average	79.6	84.2	79.4	75.6
Error	4.630335	1.939072	5.885576	5.083306
Average (Total)	79.7			
Error (Total)	5.541660401			

Concentration: 5 mg/mL				
	Sample			
	A	B	C	D
Place 1	42	39	38	41
Place 2	39	38	40	39
Place 3	41	37	38	41
Place 4	41	39	41	41
Place 5	43	41	37	38
Average	41.2	38.8	38.8	40
Error	1.32665	1.32665	1.469694	1.264911
Average (Total)	39.7			
Error (Total)	1.676305461			

Concentration: 2 mg/mL				
	Sample			
	A	B	C	D
Place 1	17	15	15	17
Place 2	17	16	17	18
Place 3	14	14	15	13
Place 4	16	17	15	
Place 5	14	16	17	14
Average	15.6	15.6	15.8	15.5
Error	1.356466	1.019804	0.979796	2.061553
Average (Total)	15.63157895			
Error (Total)	1.384520678			

Concentration: 1 mg/mL				
	Sample			
	A	B	C	D
Place 1	8	8	10	10
Place 2	8	7	9	9
Place 3	8	7	8	8
Place 4	9	8	8	8
Place 5	7	9	8	8
Average	8	7.8	8.6	8.6
Error	0.632456	0.748331	0.8	0.8
Average (Total)	8.25			
Error (Total)	0.829156198			

Concentration: 0.5 mg/mL				
	Sample			
	A	B	C	D
Place 1	5	4	4	3
Place 2	4	5	4	6
Place 3	4	4	4	5
Place 4	4	5	3	4
Place 5	3	4	5	4
Average	4	4.4	4	4.4
Error	0.632456	0.489898	0.632456	1.019804
Average (Total)	4.2			
Error (Total)	0.748331477			

Figure S20. The thickness of samples with different spin-coating concentrations

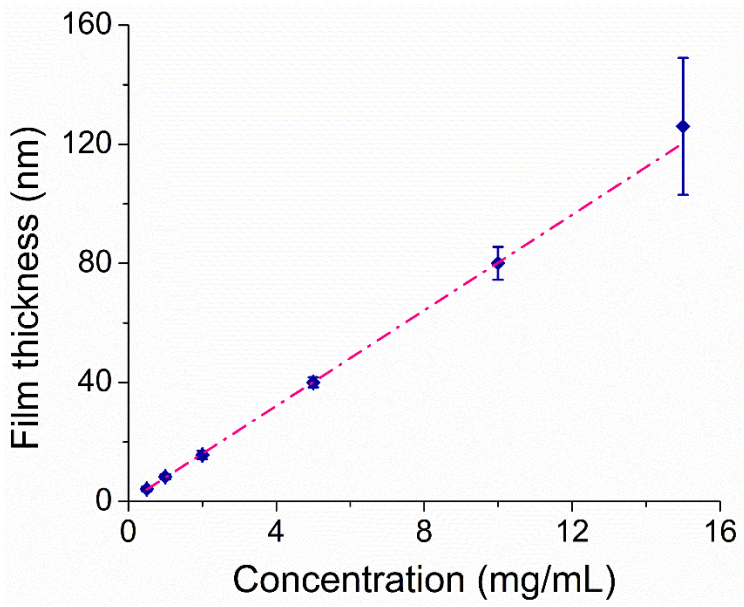

Figure S21. Thickness-concentration dependence of spin-coated films on SiO_2-covered (300 nm) silicon wafers. Standard deviations of the thickness are shown as error bars.

Top view of thin films and surface roughness measurement

The surface topology and roughness of spin-coated thin films were measured by a *Cypher S* AFM from *Oxford instruments* and analyzed with *Gwyddion* or *Cypher*.

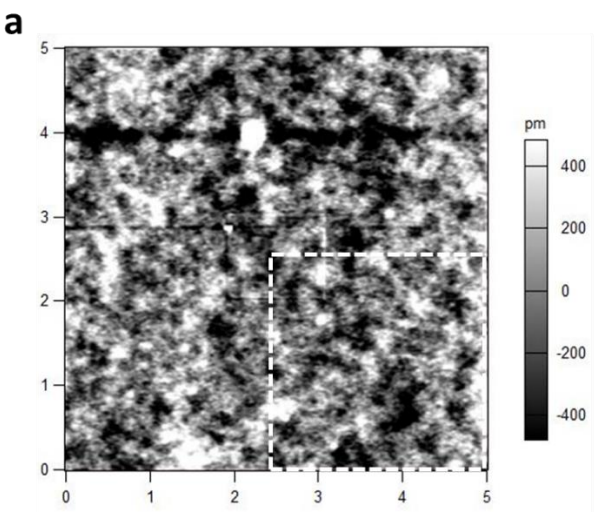

Image size	Calculated roughness*
5 * 5 μm (from **a)**	543 pm
2.5 * 2.5 μm (white square in **a)**	277 pm

* from Asylum 14.0

Figure S22. AFM topology of spin-coated **2DPA-1** film (**a**) and its calculated roughness (**b**).

All those spin-coated films have super-flat surfaces. Their roughness usually ranges from 300-400 pm over a 5*5 μm area, similar to a commercial ultra-flat silica wafer. In **Figure S22**, 543 pm of surface roughness was observed due to a white dot in the upper middle. We attribute this residue as multiple layer laminates or a 3D amorphous molecule.

The HR-AFM characterization of thin-films also offers some topologic information. However, unlike measurements of single platelets on the mica substrate, height images of thin-films are vague, probably due to the soft nature of 2D molecules and their incommensurate (random) stacking (**Figure S23a**). Fortunately, we found that the image contrast can be dramatically enhanced when the tip oscillates at higher eigenmode values.[11] Therefore, in dual AC mode, the amplitude-channel AFM image at the second eigenmode value gives a much higher sensitivity to the height variation, showing clear edges for individual molecules (**Figure S23b**). Thus, by just measuring the film surface, we can get a top-layer molecular size distribution (**Figure S17d**) which should also reflect the real bilayer distribution because during the spin-coating process, there is no molecular size preselection involved.

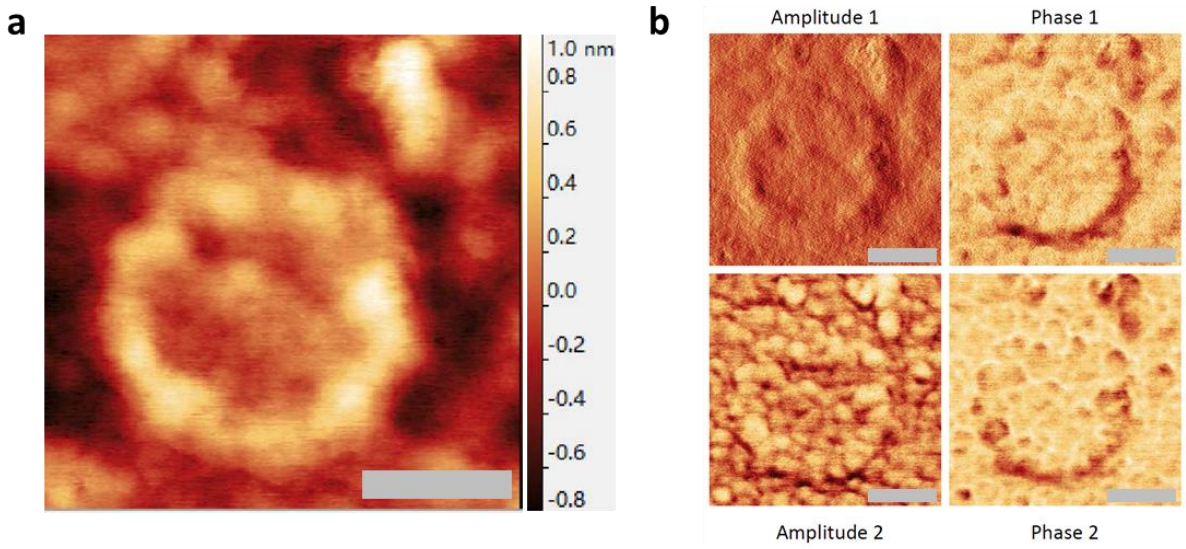

Figure S23. a, Original height image of a selected area. Scale bar: 50 nm. **b,** Amplitude and phase images at the first (up) and second (down) eigenmodes. Scale bar: 50 nm.

The cross-sectional view of thin films and thickness measurement

The uniformity and thickness of thin films can be also measured by TEM (**Figure S24**) and SEM (**Figure S25**). The TEM sample was prepared by Focused Ion Beam (FIB) cutting of a spin-coated film sample followed by mild argon milling while samples for SEM were directly observed at the fresh-cleaved substrate edge after Au sputtering of a spin-coated film sample. In SEM images, there are some **2DPA-1** debris sticking to the fractures but wouldn't affect the thickness measurement.

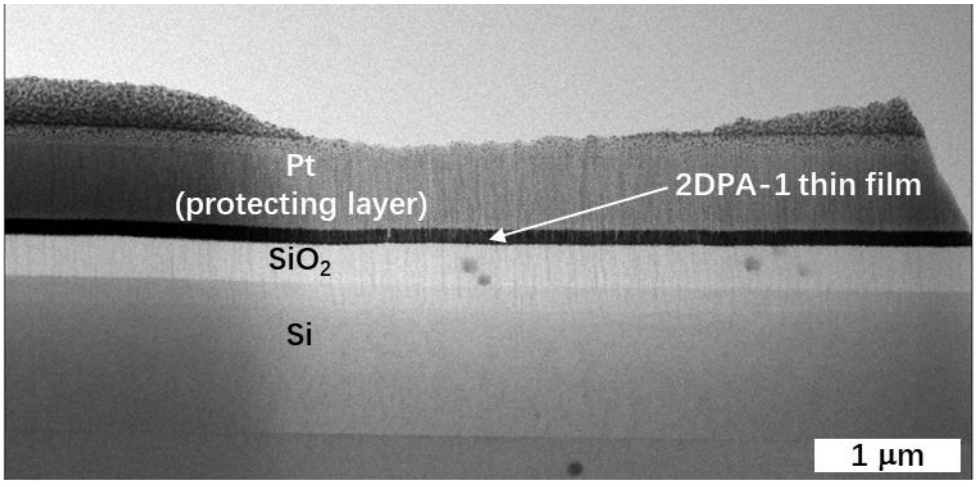

Figure S24. A cross-sectional view TEM image of **2DPA-1** thin film on a SiO_2/Si substrate. Oxide thickness: 300 nm.

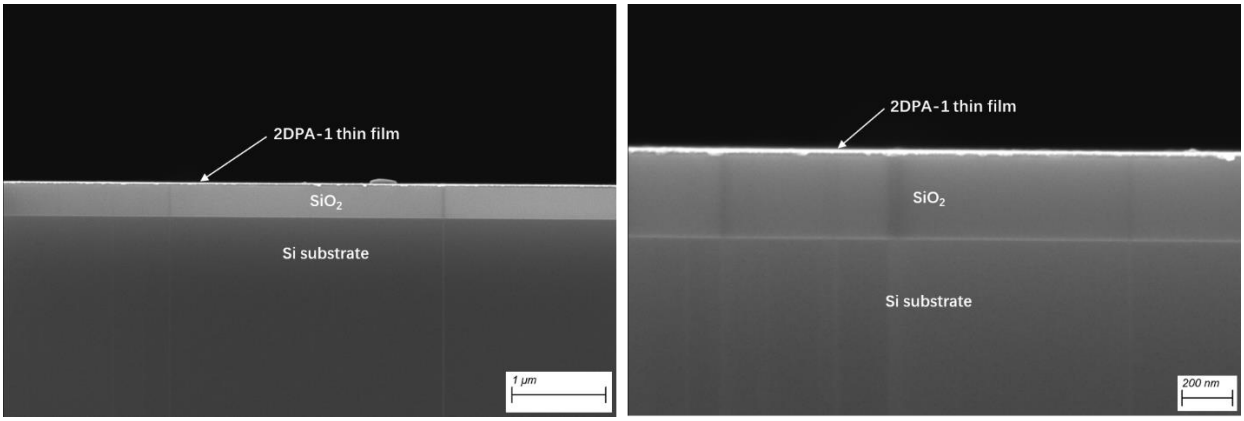

Figure S25. Cross-sectional view SEM images of **2DPA-1** thin film with different magnifications. Oxide thickness: 300 nm.

Characterizations of suspended thin films made by drop-casting

Suspended films were formed when dilute **2DPA-1** solution was drop-casted and dried on a holey TEM grid. The desired films were then characterized by SEM (**Figure S26**) and AFM (on a different sample, **Figure S27**).

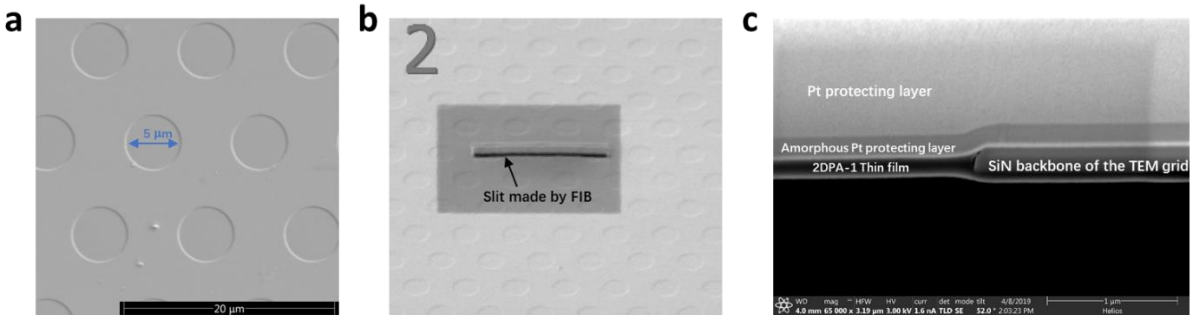

Figure S26. Top-view SEM images of suspended films before (**a**) and after (**b**) focused ion beam (FIB) cutting. **c**, Cross-sectional view of FIB cut suspended film. The hole size of the TEM grid: 5 μm.

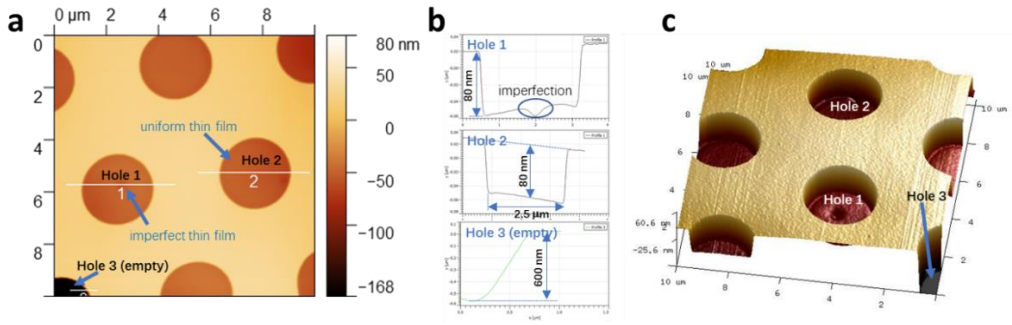

Figure S27. AFM topology (**a**), height information (**b**), and 3D reconstruction (**c**) of suspended thin films. The hole size of the TEM grid: 2.5 μm.

The suspended films first grow along the wall of the grid holes, and then cross it. This observation is similar to that of suspended graphene films and the deep of thin-film implies the strength of substrate-film affinity.[12,13]

Grazing-Incidence Wide-Angle X-ray Scattering (GIWAXS) Analysis

The transferred spin-coated nanofilm (size: around 1.5*1.5 cm; substrate: SiO_2/Si) was measured by Dr. Esther Tsai at the beamline 11-BM Complex Materials Scattering (CMS) of National Synchrotron Light Source II (NSLS-II) in the Brookhaven National Laboratory. Thin-film samples were measured at incident angle 0.12 deg with a 200um(H)*50um(V) beam at wavelength λ=0.9184 Å. 2D scattering patterns were obtained using Dectris Pilatus800k at 0.257m downstream the samples. Data analysis was carried out using beamline-developed software SciAnaylsis (https://github.com/CFN-softbio/SciAnalysis).

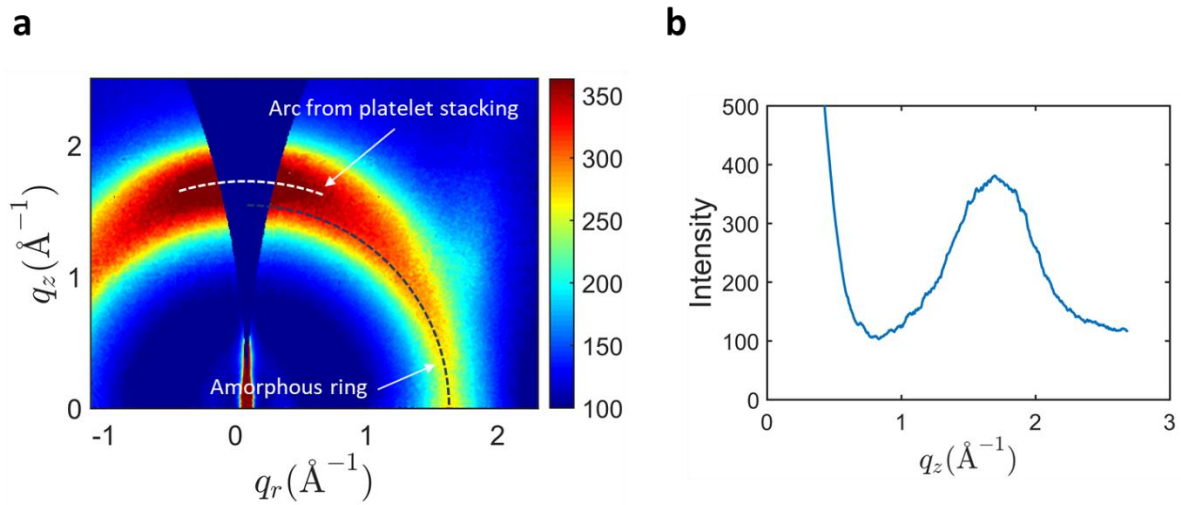

Figure S28. **a**, Grazing-incidence wide-angle X-ray scattering (GIWAXS) 2D scattering data of a **2DPA-1** thin film obtained from beamline 11-BM of the National Synchrotron Light Source II (NSLS-II). **b**, 1D intensity profile near q_r = 0 A^{-1}.

An amorphous diffraction ring is also observed at slightly smaller q_r. We reason that this amorphous peak also exists in PXRD and thus broaden and shift a little the main peak at 24.3 degree.

Gas Permeability and Accessible Free Volume from Bulge Test

In a bulge test, a thin film is suspended over a microcavity in a substrate, trapping the gas inside. If a pressure difference exists between the two sides of the thin film, it will bulge upwards or downwards, quantified by the deflection height at the center point δ. The deflection height δ can be measured by atomic force microscopy (AFM). According to Hencky's solution, the height δ is correlated with the pressure difference Δp exerting on the thin film as follows:[14-16]

$$\Delta p = \frac{16EdK(v)}{a^4}\delta^3 \quad (1)$$

where E is the Young's modulus of the thin film, d is the film thickness, $K(v)$ is a coefficient depending on the Poisson's ratio v of the film,[14] and a is diameter of the microcavity.

If the thin film is gas permeable, the gas leak rate can be calculated by monitoring the rate of $\delta(t)$ decaying to zero. Using Eq. (1), the pressure in the microcavity can be calculated as a function of time, which is then used to calculate the gas leak rate. This technique is very sensitive, and has been used to measure the gas barrier properties[12] or the ultralow gas permeances through thin films made of 2D materials.[15-18] However, this technique has rarely been applied for measuring the gas permeabilities of membranes made of 1D polymers, because they are typically high enough such that the low detection limit provided by the bulge test is not necessary.

During our study, we found that bubbles from nanoindentation samples didn't deflate even after 5 months. To get a better estimation on **2DPA-1**'s gas permeability, herein we monitored the heights of ten bubbles from two different samples, varying their film thicknesses and well diameters. The bubbles did not deflate for more than few months (**Figure S29**). The fluctuating bubble heights may be caused by drifting of the AFM system. This impermeability of **2DPA-1** in a bulge test strongly suggests that **2DPA-1** does not contain accessible free volumes similar to those in 1D polymers because, as we will show below, the air permeability of **2DPA-1** is much lower than the lowest permeability among those of 1D polymers.

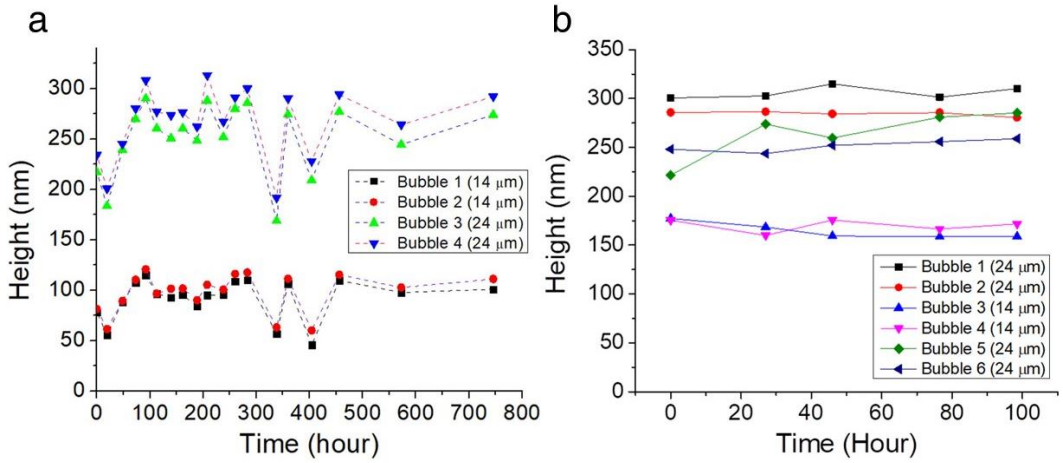

Figure S29. The heights of gas bubbles as functions of time. **a**, A substrate with four bubbles for a **2DPA-1** film of thickness 12.8 nm. **b**, A chip with six bubbles from a **2DPA-1** film of thickness 56.1 nm. (Legends contain well diameters.)

Poly(ethylene vinyl alcohol) (EVOH) is one of the most O_2-impermeable 1D polymers.[19,20] Its minimum O_2 permeability is $P(O_2) \sim 6\times10^{-5}$ barrer (1 barrer = 3.35×10^{-16} mol m m^{-2} s^{-1} Pa^{-1}). According to the Robeson upper bound for O_2/N_2 separation, the O_2/N_2 selectivity might reach ~ 100 when $P(O_2) \sim 6\times10^{-5}$ barrer, although no data points has been provided in this range.[21] Here, we consider O_2 permeability only and neglect the permeations of N_2, H_2O, and other gases to estimate the upper bound of the O_2 permeability.

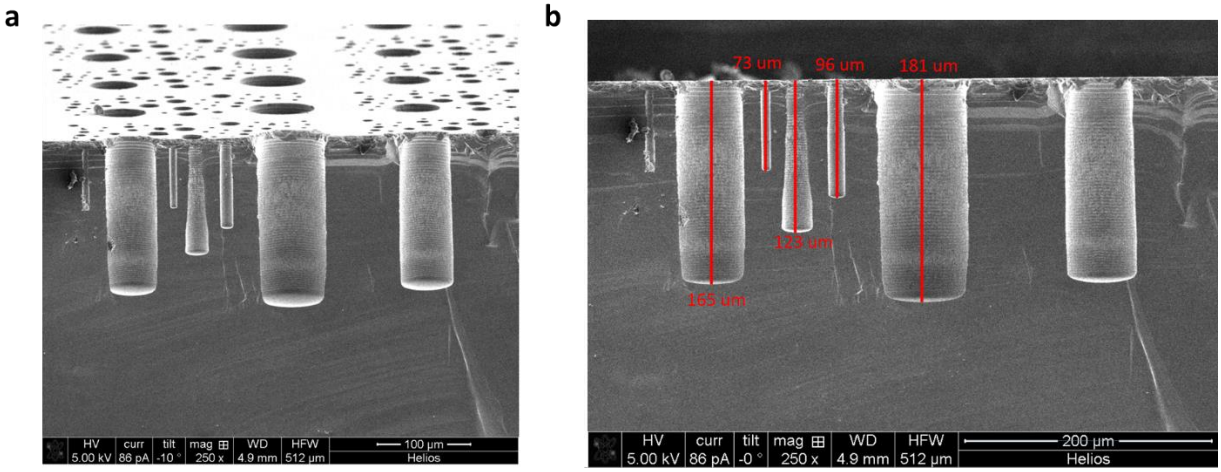

Figure S30. Measurement of well depths using SEM.

The volume of the air bubble V consists of the volume of the microcavity with no deflection V_0 and the additional volume ΔV resulting from the film deflection δ (< 400 nm). Considering the diameter a (14

and 24 μm, obtained from AFM) and the depth *h* (98 and 123 μm, obtained from SEM, showing in **Figure S30**) of the microcavity, the total volume *V* can be expressed as:

$$V = V_0 + \Delta V = \frac{\pi a^2 h}{4} + C(\nu)\frac{\pi a^2 \delta}{4} \tag{2}$$

where $C(\nu)$ is a coefficient less than 1 depending on the Poisson's ratio ν of the film. Because $\delta \ll h$, $V \approx V_0 = \pi a^2 h/4$. According to the ideal gas law, the moles of air in the bubble $n = pV_0/RT$, where p is the pressure in the bubble, R is the gas constant, and T is the temperature. Therefore, the gas leak rate $\mathrm{d}n/\mathrm{d}t$ is:

$$\frac{\mathrm{d}n}{\mathrm{d}t} = \frac{V_0}{RT}\frac{\mathrm{d}p}{\mathrm{d}t} \tag{3}$$

On the other hand, the gas leak rate is related to the O_2 permeability $P(O_2)$ as follows:

$$\frac{\mathrm{d}n}{\mathrm{d}t} = \frac{P(\mathrm{O_2})}{d}\cdot A \cdot \Delta p(\mathrm{O_2}) = -\frac{P(\mathrm{O_2})}{d}\cdot\frac{\pi a^2}{4}\cdot 0.21(p - p_0) \tag{4}$$

where d is the film thickness (12.8 or 56.1 nm), A is the area of air permeation ($A = \pi a^2/4$), $\Delta p(O_2)$ is the partial pressure difference of O_2 across the film, p_0 is atmospheric pressure, and 0.21 is the composition of O_2 in air. The permeating area change caused by the bulge can be neglected because $\delta \ll a$.

Combining Eqs. (2)–(4), a differential equation of p is obtained:

$$\frac{\mathrm{d}p}{\mathrm{d}t} = -\frac{0.21RTP(\mathrm{O_2})}{V_0 d}\cdot\frac{\pi a^2}{4}\cdot(p - p_0) = -\frac{0.21RTP(\mathrm{O_2})}{hd}(p - p_0) \tag{5}$$

The solution is:

$$p(t) = C\exp\left(-\frac{0.21RTP(\mathrm{O_2})}{hd}t\right) + p_0 \tag{6}$$

or

$$\Delta p = p(t) - p_0 = C\exp\left(-\frac{0.21RTP(\mathrm{O_2})}{hd}t\right) \tag{7}$$

where C is a constant depending on the initial condition. According to Eq. (1), the film deflection height $\delta(t)$ has a one-to-one correspondence with the pressure difference Δp in the following logarithm form:[15,16]

$$3\ln\delta(t) + \ln\left(\frac{16EdK(\nu)}{a^4}\right) = \ln(\Delta p) = \ln C - \frac{0.21RTP(\mathrm{O_2})}{hd}t \tag{8}$$

Taking the derivative of $\ln\delta(t)$ with respect to t, we can obtain the following expression to estimate the O_2 permeability of **2DPA-1**:

$$P(\mathrm{O_2}) = -\frac{\mathrm{d}\ln\delta(t)}{\mathrm{d}t}\cdot\frac{3hd}{0.21RT} \tag{9}$$

Using linear regression, we can calculate the 95% confidence interval of the slope $\mathrm{d}\ln\delta(t)/\mathrm{d}t$, and correspondingly, the 95% confidence interval of $P(O_2)$. The upper limit estimations (95% confidence level) of $P(O_2)$ of each **2DPA-1** film are listed in **Table S2.**

Table S2*. Experimental details of ten bulge tests of* ***2DPA-1*** *and their corresponding upper limits of O_2 permeability as of July 5th, 2021 for ongoing permeability experiments.*

Sample ID	Microcavity depth (μm)	Membrane thickness (nm)	Testing time (h) as of July 5th, 2021	Current upper limit of O_2 permeability $P(O_2)$* (10^{-5} barrer)	Lower limit of $P(O_2$, EVOH$)/P(O_2$, **2DPA-1**)
a-1	98	12.8	746	0.40	15.0
a-2	98	12.8	746	0.34	17.7
a-3	123	12.8	746	0.29	20.4
a-4	123	12.8	746	0.26	22.8
b-1	123	56.1	98.5	2.90	2.1
b-2	123	56.1	98.5	1.40	4.3
b-3	98	56.1	98.5	5.77	1.0
b-4	98	56.1	98.5	5.08	1.2
b-5	123	56.1	98.5	8.75	0.7
b-6	123	56.1	98.5	1.86	3.2

* 95% confidence level.

Based on the impermeability of Sample a-1 and a-2, we can bracket the O_2 permeability of **2DPA-1** below 0.26×10^{-5} barrer, which is 22.8 times lower (as of July 5th, 2021) than that of the most O_2 impermeable 1D polymer in the literature, EVOH (6×10^{-5} barrer), indicating a significant structural difference between **2DPA-1** and a hypothetical 1D polymer equivalent. *Assuming that the non-declining bubble heights continue to persist, at the current testing rate, we expect to confirm a lower limit of 65 times by Sept 2021 (additional 1500 hrs. time span). We make this prediction assuming that the standard deviation of the bubble height fluctuation remains the same.*

Alternatively, we can compare the O_2 permeabilities of **2DPA-1** and EVOH from the perspective of the time scale of bubble deflation. According to Eq. (10), the half-life of a decreasing bubble height τ is:

$$\tau = \frac{3\ln 2\, hd}{0.21RTP(\mathrm{O_2})} \tag{10}$$

If the 12.8-nm-thick film in Sample a-1 and a-2 were made of EVOH, the bubble deflation time scale τ at room temperature would be:

$$\tau = \frac{3 \ln 2 \times 98\ \mu\text{m} \times 12.8\ \text{nm}}{0.21 \times 8.314\ \text{J mol}^{-1}\ \text{K}^{-1} \times 298\ \text{K} \times (6 \times 10^{-5}\ \text{barrer})} = 2.5 \times 10^{5}\ \text{s} = 69\ \text{h}$$

Note that τ = 69 h is an upper limit of the half-life of bubble deflation if our **2DPA-1** film were indeed a 1D polymer. This upper limit can be further reduced if the permeations of other components in air (N_2, H_2O) are considered. In contrast, the gas bubble a-1 and a-2 sealed by **2DPA-1** showed no observable deflation over 750 h.

Polarized Photoluminescence (PL) Characterization

Optical setup

The whole optical setup is shown in **Figure S31**. A continuous-wave 532 nm laser (Edmund, 35-072) was used for excitation. The incident light travelled through a linear polarizer and a half-wave plate (mounted on a motorized stage) and focused onto the sample using an objective lens (Zeiss, 100x, NA=0.75). The angle of the half-wave plate was adjusted to maximize photoluminescence intensity. Then, the stage was moved a few μm away because **2DPA-1** has already photobleached to some extent during the focusing and adjustment of the half-wave plate. The signal was collected with a spectrometer (Princeton Instruments, Acton SpectraPro SP-2150, and PyLon). The excitation power for photoluminescence measurements was 500 μW and the exposure time was 10 seconds. For simple PL measurement, a spectrometer was used for data collection. However, for the polarized PL study, we used an EMCCD camera (Andor, iXon3), which is much more sensitive, to trace a longer time course despite the photobleaching of **2DPA-1**. The polarity of the incident light was controlled by rotating the half-wave plate and the PL signal was collected every 5 degrees with 5 seconds exposure time. The excitation power was 2 μW for excitation polarization. All measurements were conducted at room temperature under air.

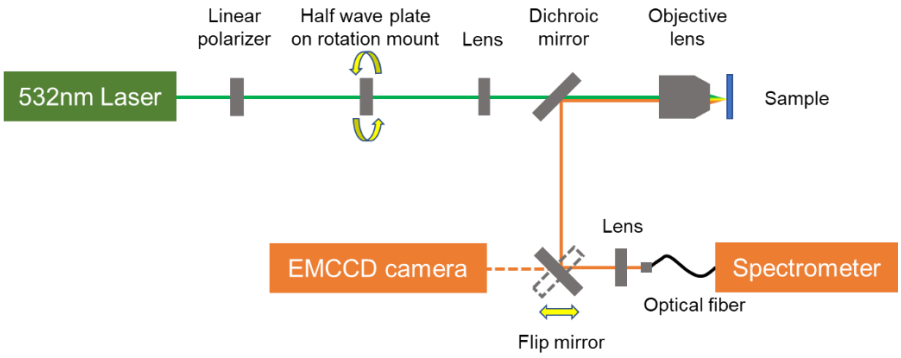

Figure S31. Optical setup for Photoluminescence measurements

Sample preparation and mounting

First, spin-coat **2DPA-1** films onto clean SiO_2/Si substrates. For top view measurement, the sample was fixed onto a glass slide with a flat-on orientation. To protect the **2DPA-1** film from scratching and contamination, the film side was facing the glass slide. For side view measurement, the sample was cut into two pieces. The freshly cleaved edge was glued onto a glass slide with an edge-on orientation. The film is perpendicular to the glass slide.

Photoluminescence measurement

Before the polarized PL study, we measured PL spectra of **2DPA-1** in bulk powder, solution-phase (10 mg/mL), and different oriented samples (**Figure S32**).

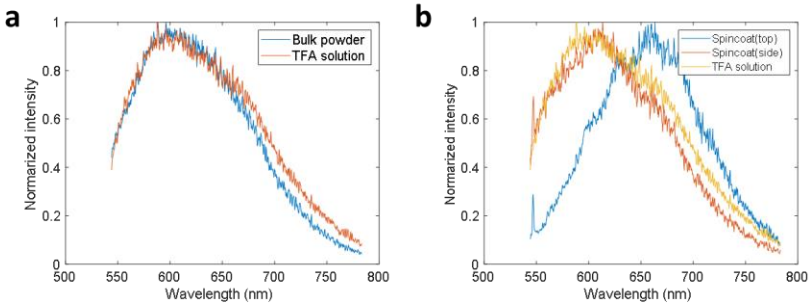

Figure S32. **a**, A comparison of Photoluminescence data from bulk powder and TFA solution. **b**, Photoluminescence response from top view sample, side view sample, and TFA solution.

The fact that both bulk powder (condensed state) and TFA solution (highly dispersed state) offer the same PL response indicates that individual molecule excites and emits on its own, without any synergy. The difference between the top view and side view shows the existence of different excitation modes, which are sensitive to the incoming laser pathway.

Polarized photoluminescence study

Data was collected using an EMCCD detector. Linear polarization is controlled by rotating a half-wave plate.

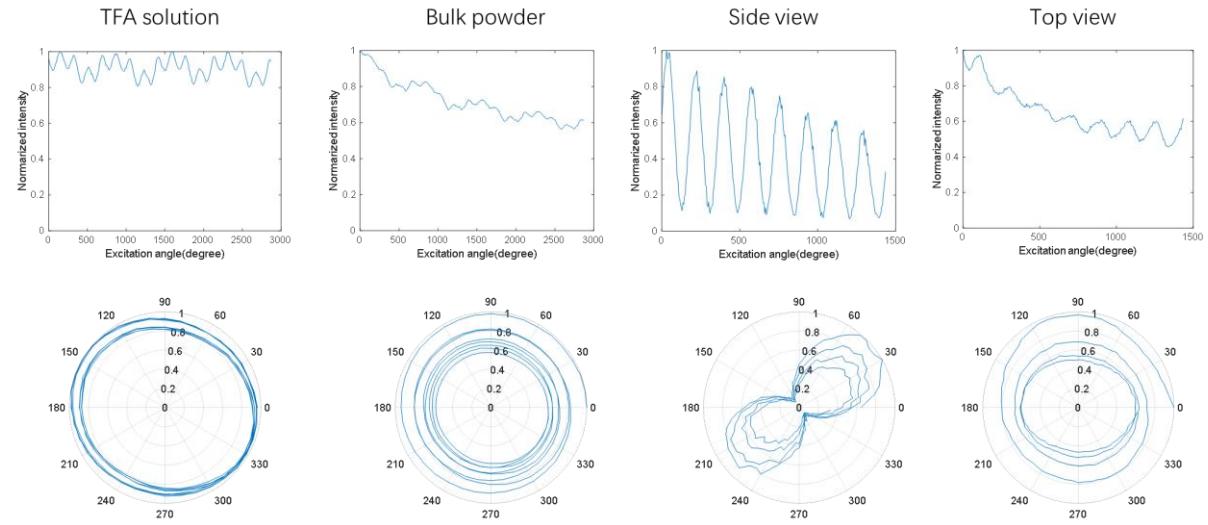

Figure S33. Photoluminescence intensity-excitation angle curves (up) and their corresponding polar plots (bottom).

Only the side view sample shows angular dependence, indicating that **2DPA-1** molecules are anisotropically aligned in *yz* plane. Likewise, the lack of angular dependence implies that **2DPA-1** molecules are isotropically dispersed in *xy* plane. The intensity decrease observed in bulk powder, top view, and the side view is attributed to photobleaching of **2DPA-1**, probably originate from laser heating. After fitting and normalizing data with an exponential decay (from first-order kinetics), bleaching corrected data was shown in **Figure S34**.

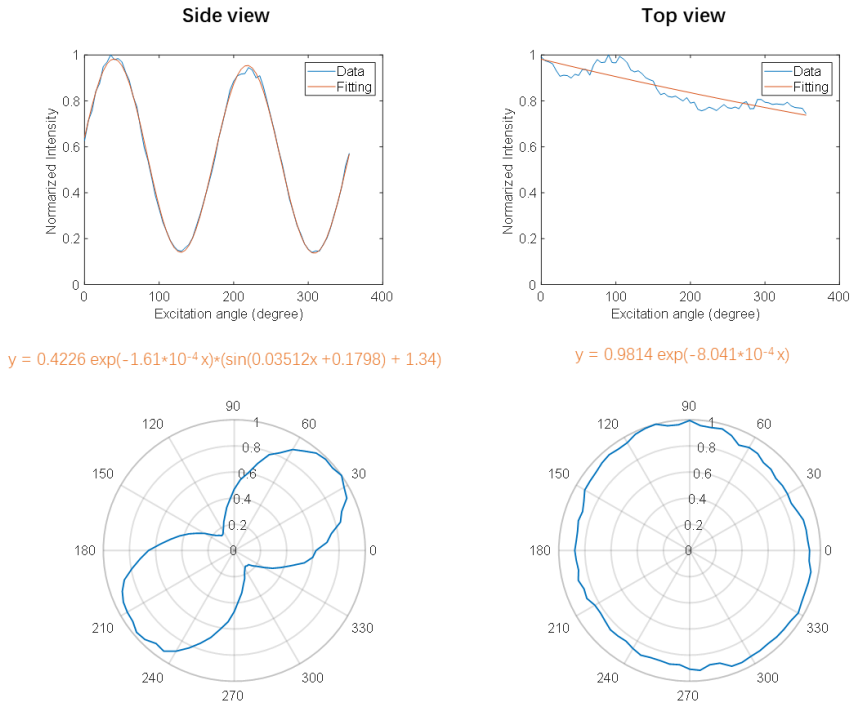

Figure S34. Fit the PL intensity with first-order decay (up). Normalized polar plots (bottom) of the side view (left column) and top view (right column).

Structure optimization

We used periodic density functional theory (DFT) with the plane-wave code Quantum-ESPRESSO to simulate the theoretical in-plane structure of the **2DPA-1**. The plane-wave code, QUANTUM ESPRESSO, was used to determine the lattice constants. The generalized gradient approximation (GGA) with the PBE exchange-correlation functional was applied in conjunction with D3 semi-empirical dispersion to determine lattice constants. Norm-conserving pseudopotentials were employed for all elements with 2s and 2p states in the valence (i.e., for C, N, O) or 1s states in the valence (i.e., H). A plane wave kinetic energy cutoff of 680 eV was employed along with default energy convergence and force thresholds of 10^-4 eV and 10^-3 eV/A, respectively. Lattice constants were determined by relaxing ionic positions and using variable cell relaxation with the same Monkhorst-Pack k-point sampling of 8 × 8 × 4.

In **Table S2**, we rotated the two layers of the structures to generate initial structures of possible in-plane bi-layered structures. Taking a **2DPA-1** unit cell as the first layer, we placed the second layer in different orientations. We rotated the two layers with respect to each other from 0˚ to 180˚ and 3.45 Å away from the first layer. We carried out variable cell relaxation and successfully obtained 22 structures with converged results (see Methods below) and a realistic cell was obtained.

Table S2. The optimal lattice parameters (a, b, c, in Å and α, β, and γ in °) interlayer distance (d in Å), and relative total energy of calculated in-plane **2DPA-1** structures (in kcal/mol). The relative energy is reported with respect to the structure with the lowest energy of the 22 calculated structures.

Structures	a (Å)	b (Å)	c (Å)	α (˚)	β (˚)	γ (˚)	d (Å)	Relative energy (kcal/mol)
1	11.06	11.04	6.94	87.91	91.12	119.82	3.47	0.00
2	11.07	11.06	6.96	90.58	88.48	120.01	3.48	1.54
3	11.07	11.09	6.95	89.19	90.57	120.01	3.48	1.61
4	11.09	11.06	6.93	90.60	89.31	119.80	3.47	1.84
5	11.02	11.04	6.96	89.41	92.12	119.91	3.48	3.28
6	11.02	11.03	6.95	89.24	92.05	119.89	3.48	3.36
7	11.10	11.03	6.99	86.91	88.73	120.61	3.50	3.40
8	11.10	11.03	6.99	86.91	88.73	120.61	3.50	3.40
9	11.10	11.03	6.99	86.91	88.73	120.61	3.50	3.40
10	11.11	11.09	7.00	89.98	90.00	119.92	3.50	3.57
11	11.11	11.11	7.00	90.02	90.09	120.15	3.50	3.58
12	11.11	11.09	6.99	89.98	90.01	119.90	3.50	3.58
13	11.11	11.08	7.00	90.00	89.99	119.89	3.50	3.58

14	11.09	11.07	6.92	90.08	89.69	119.94	3.46	3.63
15	11.09	11.07	6.92	90.08	89.69	119.94	3.46	3.77
16	11.09	11.07	6.92	90.08	89.69	119.94	3.46	5.53
17	11.08	11.07	7.22	90.09	90.02	119.83	3.61	6.24
18	11.07	11.07	7.22	90.10	89.98	119.81	3.61	8.23
19	11.08	11.11	7.20	89.97	90.01	120.01	3.60	8.28
20	11.10	11.09	7.18	89.98	90.05	119.94	3.59	8.38
21	11.10	11.09	7.18	90.01	89.98	119.89	3.59	8.38
22	11.10	11.09	7.18	89.98	90.05	119.94	3.59	8.41

In such a flat structure, the interlayer spacing is 3.47 Å, similar to that of graphene[22] and hBN[23] but smaller than our real interlayer spacing (3.72 Å from GIWAXS). This suggests that in the **2DPA-1**, amides are not totally flat and pointing outside of the surface, forming interlayer hydrogen bonding. In such a case, one would expect local surface charges and out-of-plane dipoles. This phenomenon has been observed in 1D systems. For instance, in Kevlar, the amide planes and aromatic cores are not within a same plane.[9,24] Instead, all amide bonds tilt to certain degrees, resulting from steric hindrance between amides and ortho substitutions (H) on the benzene rings.

Density estimation: For the most stable in-plane structure (structure 1 in **Table S2**), its mass density can be calculated as

$$r_m = \frac{\sum_{i}^{C,N,H,O} n_i M_i}{N_A V_{cell}}$$

where ρ_m is the mass density of the structure, n_i and M_i is the number of elements, i, and molar mass of element i with i representing C, N, H, and O. V_{cell} is the cell volume, and N_A is the Avogadro's number.

A mass density of 1.28 g/cm^3 was calculated and shown in **Table S3**. Since the real structure of **2DPA-1** has a larger interlayer spacing, the real mass density of **2DPA-1** should be smaller than this calculated density. Thus, this density from an entirely in-plane and densely packed structure can serve as a boundary (upper limit) for the real mass density of **2DPA-1**.

Table S3: The mass density of the predicted in-plane structure.

Cell Volume(V_{cell})	n_C	n_H	n_N	n_O	ρ_m
734.29 Å^3	24	12	12	6	1.28 g/cm^3

Estimated density ratio of steel (structural steel, ASTM A36) and **2DPA-1**: 7.85/1.28 = 6.13

Mechanical Measurements

The 2D Young's modulus (E^{2D}) and yield strength (σ^{2D}) were measured at MIT and verified by Army Research Laboratory. The scrolled fiber test was done at MIT.

AFM Nanoindentation

Materials: A Cypher AFM is used for nanoindentation. Si holey substrates were made by photolithography. Diamond-like spheric probes (Biosphere NT_B50_v0010 and NT_B100_v0010) were purchased from Nanotool AFM Probes. Tip radius information (50±5 nm and 100±10 nm) were obtained from the vendor (**Figure S35**). Their spring constants and deflection inVOLs were manually calibrated on the same AFM and then verified with a flat, thick polystyrene film on Si/SiO_2 wafer. **2DPA-1** nano thin films were either formed in situ or transferred onto the substrates. Films thicknesses were obtained by taking an average at 7 different positions nearby the place of interest.

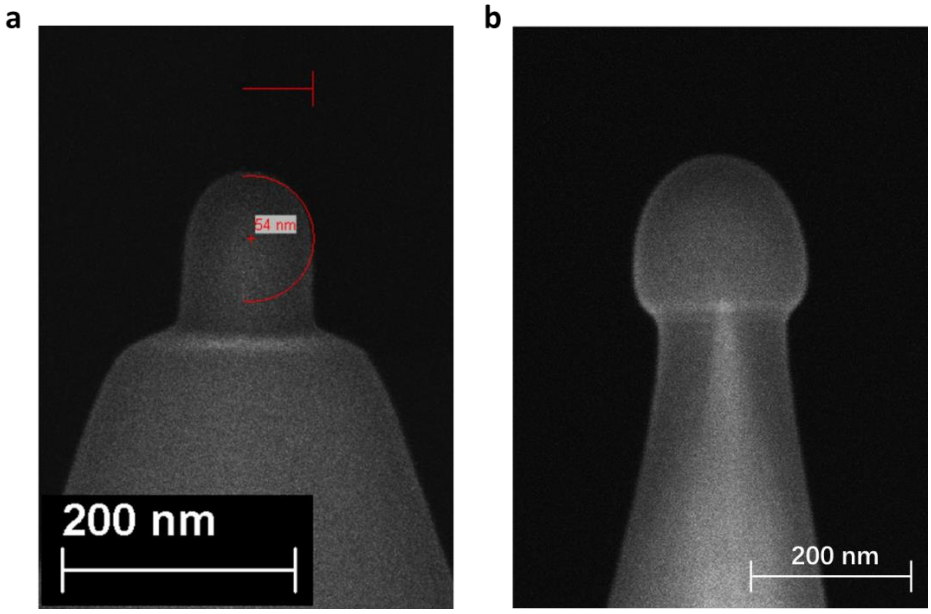

Figure S35. Images of tip heads and their radius information (from the vendor).

Film transferring method: Due to the strong interaction between the polar **2DPA-1** molecules and SiO_2 surface, one may not peel the **2DPA-1** nanofilm off from a SiO_2 substrate without destroying it. However, we can pre-lay a supporting polymer layer beneath and peel the whole composite nanofilm off from the substrate. The composite film can be trimmed, cut, and transferred to whatever substrates (different materials, different shapes) after flipping, with the polymer layer facing outside. Subsequent organic solvent washing removes the supporting polymer, leaving a **2DPA-1** film alone on the new substrate. This method can easily handle nanofilms up to 6 inches and can afford free-standing membranes across large wells up to 70 μm.

The homogeneity and flatness of transferred films were demonstrated by AFM, measured at the film edges, near which cracks, wrinkles, and folds are observed (**Figure S36a&c**). Again, the film shows a very smooth surface and a steady thickness of 7 nm (**Figure S36b**).

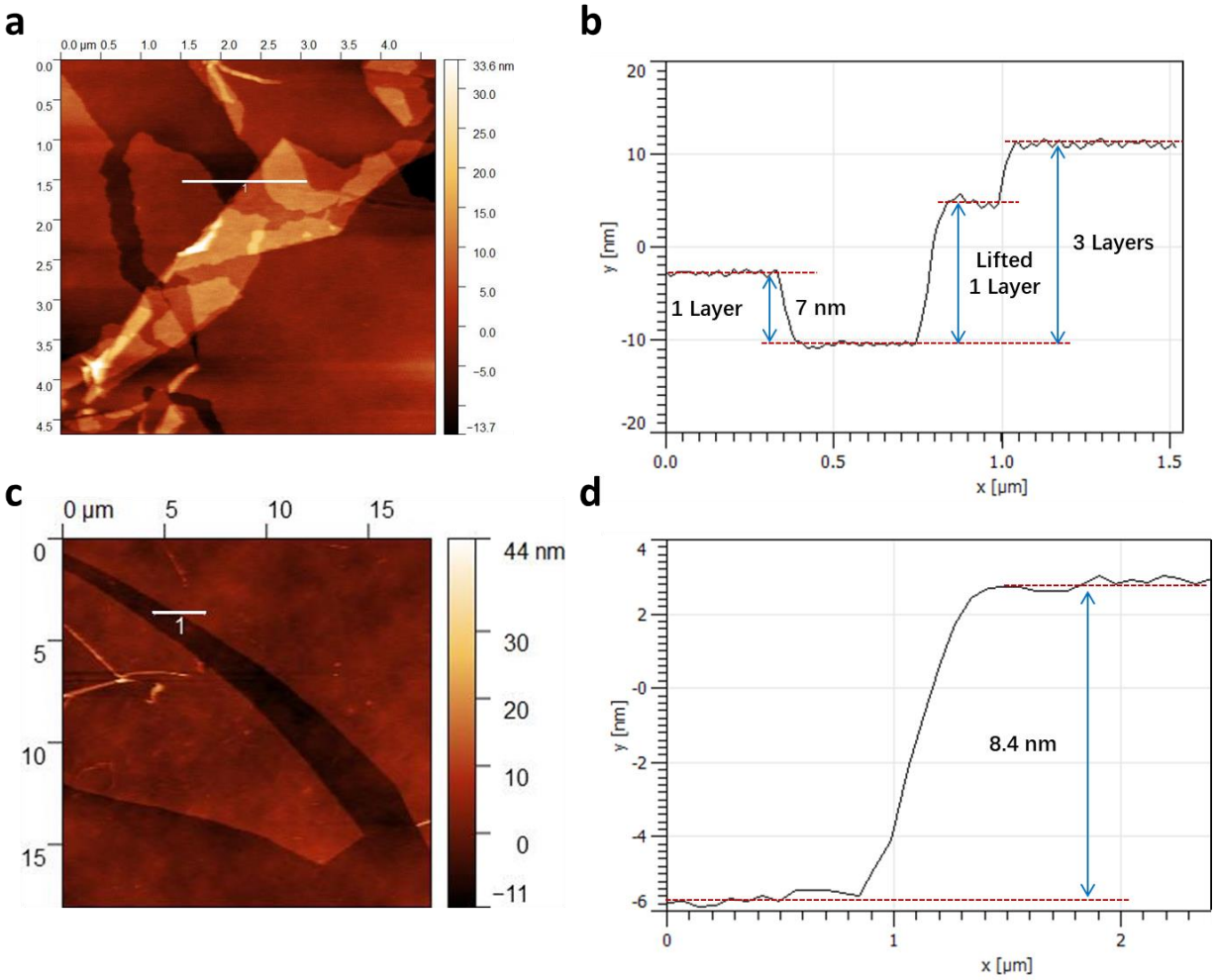

Figure S36. AFM images of two transferred **2DPA-1** films on SiO_2/Si substrates (**a**, **c**) and their height profiles (**b**, **d**) along white lines in **a** and **c**. Measured at cracks near the film edges.

Method: The AFM nanoindentation is performed on suspended membranes sitting on holey substrates (**Figure S37a**). Two samples with different film thicknesses (33.9 nm and 12.8 nm, measured from 7 different places nearby) were prepared and tested (**Figure S37b**). Nanoindentation was performed on 14-um and 24-um membranes, using two types of probes (synthetic diamond, spheric tips with a radius of 50±5 nm or 100±10 nm). Probes were calibrated manually with a bare substrate surface and verified with a thick, flat polystyrene film.

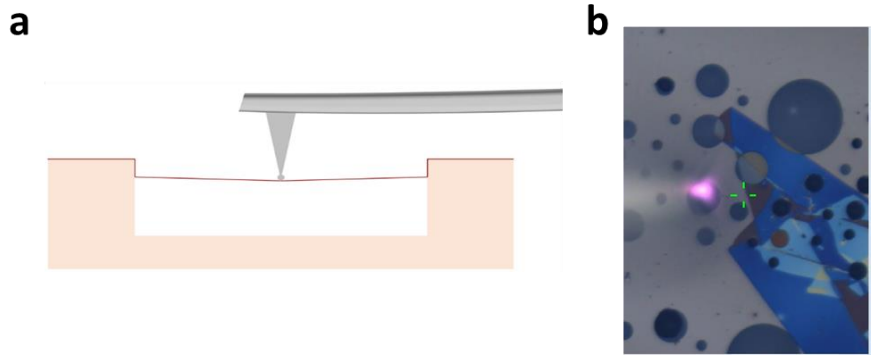

Figure S37. **a**, Schematic illustration of nanoindentation with a spheric probe on a suspended nanofilm. **b**, Thickness measurement for nanoindentation.

120 membranes were measured in total. For each membrane, multiple force-displacement curves with different trigger forces were obtained at the membrane center after releasing gas captured underneath the film. All force curves were plotted in one scheme and their elastic region (the area that curves overlap) was picked out and fitted with the following equation to get the 2D Young's modulus (E^{2D}) (**Figure S38**).[13]

$$F = \sigma_0^{2D}(\pi a)\left(\frac{\delta}{a}\right) + E^{2D}(q^3 a)\left(\frac{\delta}{a}\right)^3$$

Where σ_0^{2D} is the film pretension, δ is the deflection at the center point, a is the membrane radius, and q is a dimensionless constant calculated from Poisson's ratio ν.

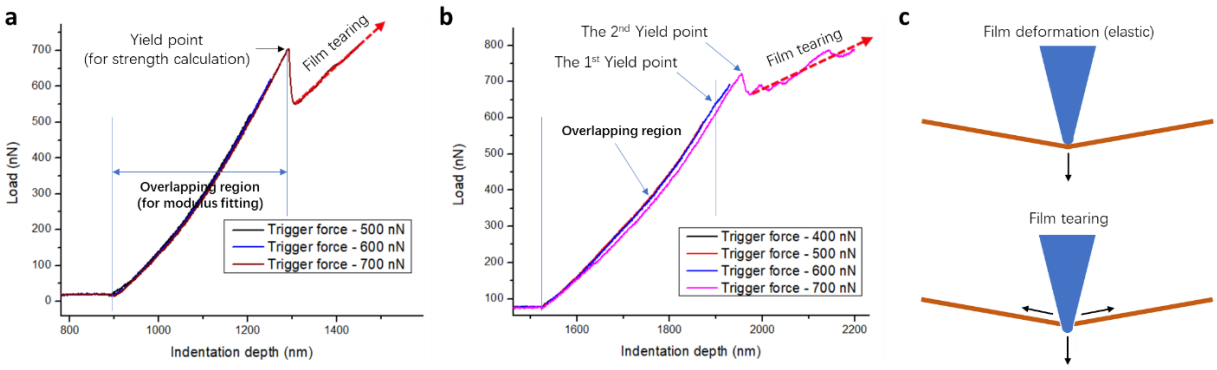

Figure S38. Determining the elastic region and yield point for force-displacement curves. **a,** Force curves with a clear yield point. **b,** Force curves with an inconspicuous yield point. **c**, Schematic illustration of elastic deformation and tearing of films.

The 2D yield strength (σ^{2D}) can be calculated from:

$$\sigma^{2D} = (FE^{2D}/4\pi R)^{1/2}$$

Where F is the force at the first yield point and R is the tip radius. Sometimes the first yield point may be vague and hard to pick out. However, in such a scenario, a right-shift in the force curve could serve as an indicator that a slight yield happened in the previous force curve.

During the mechanical measurement, we observed no ultimate failure in the entire force distance but continuous film tearing after partial failure(s), showing as a linear raise of the stress as the indentation depth increases (proportion to the increasing in hole perimeter).

The average modulus of **2DPA-1** is 12.7 GPa, with a standard deviation of 3.8 GPa. While modulus scatters from 8 to 22 GPa, strength is more condensed from 0.35-0.7 GPa, giving an average of 0.488±0.057 GPa.

The mechanical properties and gas permeability of the cast **2DPA-1** films are remarkably consistent, suggesting that voids in the as-synthesized powders (generated during polymerization) do not translate into the resulting film structure or its mechanical properties. Note that the processing involves dissolving the powder in trifluoroacetic acid that deconstructs the original structure entirely, resulting in a highly dispersed solution in which mostly bilayers are solubilized. However, the subsequent spin-coating process appears to realign 2D molecules into layered films and a global film orientation is formed.

Scrolled Fiber Tensile Test

Preparation of composite scrolled fibers: Polycarbonate (PC, Mw: 60K) solutions with different concentrations (1-4% in $CHCl_3$) were spin-coated onto clean SiO_2/Si wafers. After annealing at 100 °C, an additional layer of **2DPA-1** was introduced by spin-coating and annealing. The resulting composite nanostructures were further scrolled under transverse force to offer desired scrolled fibers (**Figure S39**).[25] All fibers were vacuum dried at 65 °C for 10 h before the test.

Note: The wafers we used herein have a uniform size of 3.5*4.5 cm. After spin-coating of the PC film and the **2DPA-1** film, the edge of the composite film is trimmed with a razor blade and the film size is 2.8*3.9 cm. In this study, the scrolling is always along the long axis. So, the length of the resulting fiber is around 2.8 cm (gauge length: 1.6 cm).

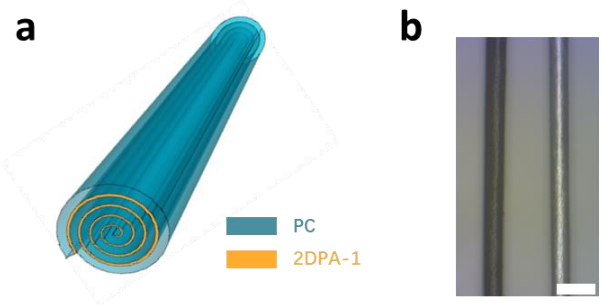

Figure S39. **a**, Schematic illustration of a composite scroll fiber. **b**, Micrograph of a human hair (left) and a scroll fiber (right). Scale bar, 100 μm.

Thickness measurement: The thickness of PC films was determined by an *XLS-100* ellipsometer from *J.A. Woollam Co.* (**Figure S40**). **2DPA-1** films were spin-coated on PC films, then transferred and washed with $CHCl_3$. The thickness of **2DPA-1** films was then determined by an AFM at scratches in 8 different places.

Spin-coating condition **I**: 2.5 mg/mL, 1500 rpm, 1min; then 100 °C, 1 min.

The thickness of **2DPA-1** film: 8.5±1.37 nm (from 8 different places)

Spin-coating condition **II**: 5.0 mg/mL, 1000 rpm, 1min; then 100 °C, 1 min.

The thickness of **2DPA-1** film: 21.1±1.90 nm (from 8 different places)

a

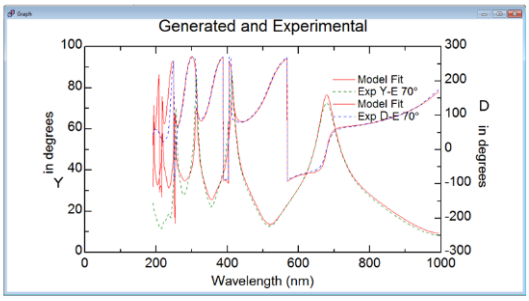

b

Concentration	Thickness
4%	912.4 nm
2%	305.6 nm
1.5%	252.4 nm
1%	137.6 nm

Figure S40. **a**, Experimental data from ellipsometer (blue curves) and its thickness fitting (red curves). **b**, Thickness of PC films with different PC concentrations. Spin-coating conditions: 4000 rpm, 1 min; then annealed at 100 °C for 4 min.

The volume fraction (V_{2DP}) can be determined as:

$$V_{2DP} = \frac{Thickness_{2DP}}{Thickness_{PC}}$$

Scroll fiber tensile test: The tensile test was performed on an *Instron 8848 Micro Tester*. Firstly, the scrolled fiber was glued onto a hollow cardboard using epoxy resin, with a gauge length of 16mm (**Figure S41a**). Then mount the whole sample onto the Instron micro tester, cut the connecting parts on the cardboard and let the scroll fiber free-stand. The test was carried out at room temperature with a strain rate of 0.1 mm/s using a 10-N load cell. The force-displacement curve is recorded until the fiber breaks off (**Figure S41b**).

a **b**

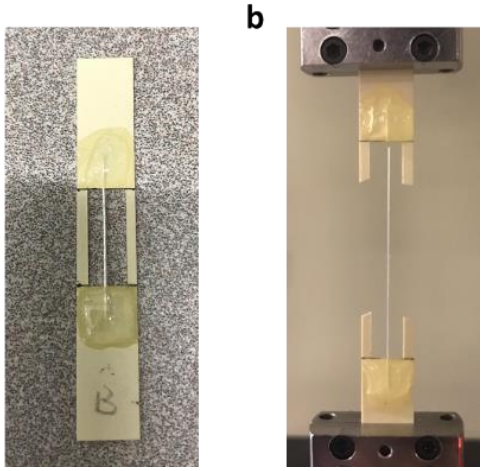

Figure S41. **a**, Before the tensile test. **b**, After the tensile test.

Data analysis: The engineering strain (ε_E) is calculated from the elongation and the original fiber length (16 mm). Meanwhile, the engineering stress (σ_E) is obtained by dividing the force by the fiber cross-sectional area, which equals to the thickness of the composite film times its length.

The true strain (ε_{tr}) and the true stress (σ_{tr}) can be converted from their engineering strain and stress, using the following equations:

$$\varepsilon_{tr} = \ln(1+ \varepsilon_E);$$

$$\sigma_{tr} = \sigma_E(1+ \varepsilon_E)$$

The elastic modulus (*E*) is calculated from the very first part (<2%) of the stress-strain curve, in which the curve is linear. The ultimate tensile strength (σ) is obtained from the failure point.

By combining different PC and **2DPA-1** spin-coating conditions, we prepared and measured composite fibers with five different volume fractions (0.9%, 2.3%, 6.9%, 7.7%, and 13.3%). The results are shown below, along with their PC control fibers (**Figure S42**).

We also compared these **2DPA-1**/PC composite scroll fiber results with our previous scroll fiber results from graphene/PC composites (**Figure S43**).[25] The graphene also shows a significant increase in strength even at a very low volume fraction (0.2%), indicating a higher enhancement efficiency. However, it decreases the fiber tensile modulus dramatically. This is attributed to the telescoping effect (**Figure S44**), which is common in 2D material/polymer composite scroll fibers.[25,26] In the **2DPA-1**/PC case, due to the highly polarized surfaces, **2DPA-1** molecules are not only binding tightly with each other, but also very "sticky" to the PC film surface. This strong inter-material interaction would be crucial for further composite development.

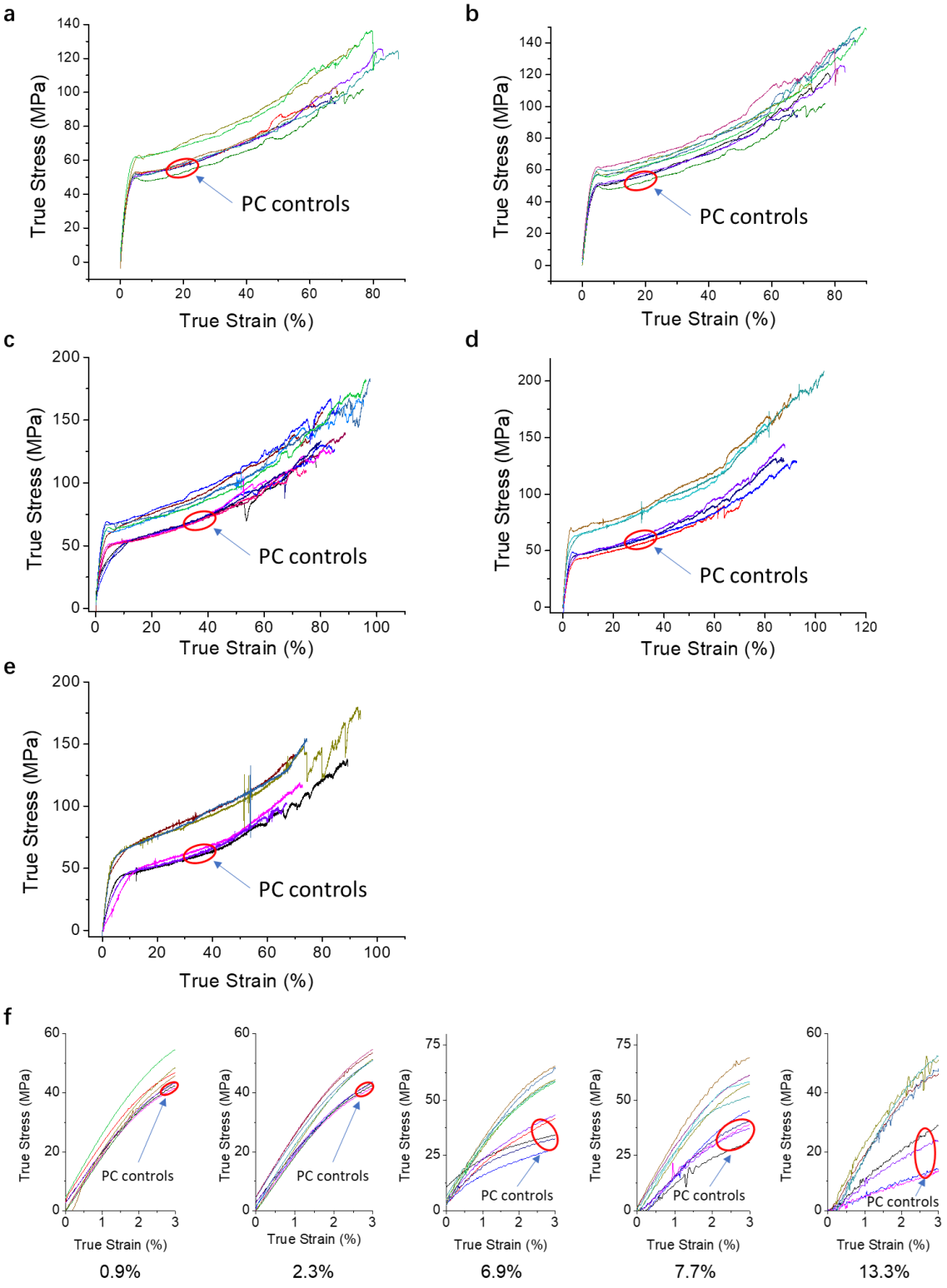

Figure S42. True stress-strain plots of composite scroll fibers and their PC controls. **a**, V_{2DP} = 0.9%. **b**, V_{2DP} = 2.3%. **c**, V_{2DP} = 6.9%. **d**, V_{2DP} = 7.7%. **e**, V_{2DP} = 13.3%. **f**, Zoomed-in images for elastic modulus calculation. Strain increment range for linear fitting: 0-2%.

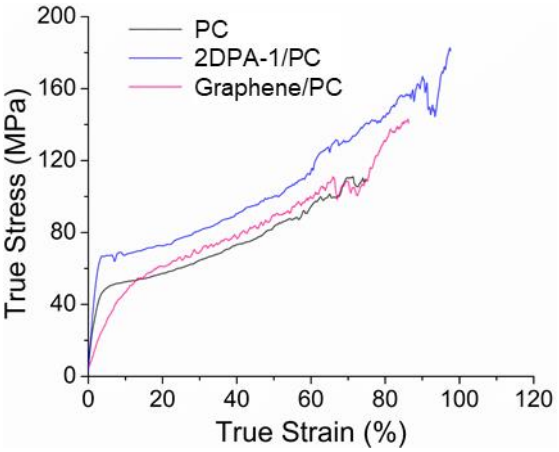

Figure S43. A comparison between a **2DPA-1**/PC scroll fiber and a graphene/PC scroll fiber, PC control is also shown. Volume fraction of **2DPA-1**: 6.9%; volume fraction of graphene: 0.19%. Graphene/PC data is reproduced from ref 25.

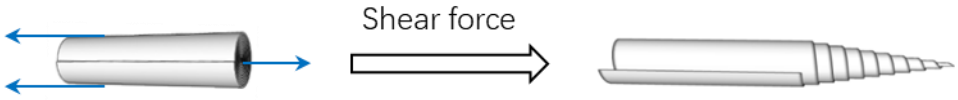

Figure S44. Telescoping under a shear force.

Chemical AFM

Chemical force mapping was performed on a *Bruker* Veeco Multimode 8 instrument. To eliminate the influence of the surface water layer and contaminations, all peak force measurements were done under fluid mode using a liquid cell. Deionized water was used as an experimental medium. Gold coated AFM probes were modified by sodium 3-mercapto-1-propanesulfonate in EtOH. To eliminate the influence from different probes, experimental results, including substrate controls, were obtained in one measurement without changing the probe.

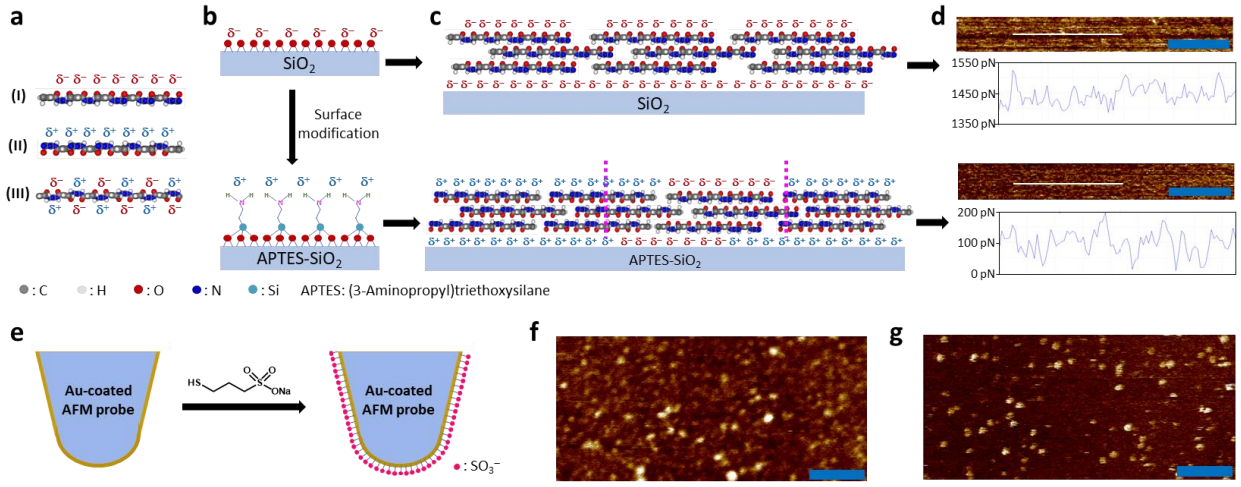

Figure S45. **Chemical force characterization of 2DPA-1 nanofilms. a,** A schematic representation of molecular surface recognition. In this molecular model, all amides are drawn vertically for better illustration. (I) Isotactic 2D molecule, negatively charged face; (II) Isotactic 2D molecule, positively charged face; (III) Syndiotactic 2D molecule. **b,** Chemical modification of SiO_2 substrate flips the surface charge from negative (top) to positive (bottom). **c,** Surface recognition can be extended from the substrate surface to the film surface. Top: **2DPA-1** film on SiO_2; bottom: **2DPA-1** film on APTES-SiO_2. However, an imperfection modification could cause a local molecular flipping on the top surface (illustrated between the two pink dashed lines). **d,** Chemical force mapping of **2DPA-1** films on SiO_2 (top) and APTES-SiO_2 (bottom) substrates. Adhesion profiles along white lines are also given under images. Scale bar, 100 nm. **e,** Surface chemical modification of a gold-coated AFM probe. **f**, Height image of a given area from a **2DPA-1** film on APTES-SiO_2 and its correlated adhesion force image (**g**). **f** and **g** were obtained simultaneously in one single scan under force mapping mode. Scale bar, 200 nm.

Note: Our chemical AFM and polarized PL target different functional groups and substructures in the **2DPA-1** nanofilm. For chemical AFM, we are studying the accessible amide bonds on the film surfaces, mainly those out-of-plane and hydrogen bondable amides. Although the result suggests that significant numbers of amide bonds are vertical and form interlayer hydrogen bonding with upper and lower layers, one cannot rule out the possibility that some of them are nearly in-plane and conjugate with adjacent Ar cores. On the contrary, chromophores in the polarized PL experiments are aromatic cores (perhaps enhanced by conjugated in-plane amides) when excited with a 532 nm laser. Unlike hydrogen bonding that is out-of-plane, these chromophores may stay roughly in-plane and are in parallel with the substrate surface, showing isotropy in *xy* plane but anisotropy in *yz* plane.

References

1 Kandambeth, S., Dey, K. & Banerjee, R. Covalent Organic Frameworks: Chemistry beyond the Structure. *J Am Chem Soc* **141**, 1807-1822, doi:10.1021/jacs.8b10334 (2019).

2 Burke, D. W. *et al.* Acid Exfoliation of Imine-linked Covalent Organic Frameworks Enables Solution Processing into Crystalline Thin Films. *Angewandte Chemie* **59**, 5165-5171, doi:10.1002/anie.201913975 (2020).

3 Smith, R. M. & Hansen, D. E. The pH-rate profile for the hydrolysis of a peptide bond. *Journal of the American Chemical Society* **120**, 8910-8913, doi:DOI 10.1021/ja9804565 (1998).

4 Brown, R. S., Bennet, A. J. & Slebocka-Tilk, H. Recent perspectives concerning the mechanism of H3O+- and hydroxide-promoted amide hydrolysis. *Accounts Chem Res* **25**, 481-488, doi:10.1021/ar00023a001 (2002).

5 Picken, S. J., Vanderzwaag, S. & Northolt, M. G. Molecular and Macroscopic Orientational Order in Aramid Solutions - a Model to Explain the Influence of Some Spinning Parameters on the Modulus of Aramid Yarns. *Polymer* **33**, 2998-3006, doi:Doi 10.1016/0032-3861(92)90087-D (1992).

6 Gong, X. *et al.* Single-Particle Tracking for Understanding Polydisperse Nanoparticle Dispersions. *Small* **15**, e1901468, doi:10.1002/smll.201901468 (2019).

7 Hu, X., Kaplan, D. & Cebe, P. Determining beta-sheet crystallinity in fibrous proteins by thermal analysis and infrared spectroscopy. *Macromolecules* **39**, 6161-6170, doi:10.1021/ma0610109 (2006).

8 McQuade, D. T., McKay, S. L., Powell, D. R. & Gellman, S. H. Indifference to Hydrogen Bonding in a Family of Secondary Amides. *Journal of the American Chemical Society* **119**, 8528-8532, doi:10.1021/ja9711019 (1997).

9 Northolt, M. & Van Aartsen, J. On the crystal and molecular structure of poly-(p-phenylene terephthalamide). *Journal of Polymer Science: Polymer Letters Edition* **11**, 333-337 (1973).

10 Patterson, A. L. The Scherrer Formula for X-Ray Particle Size Determination. *Phys Rev* **56**, 978-982, doi:10.1103/PhysRev.56.978 (1939).

11 Korolkov, V. V. *et al.* Ultra-high resolution imaging of thin films and single strands of polythiophene using atomic force microscopy. *Nat Commun* **10**, 1537, doi:10.1038/s41467-019-09571-6 (2019).

12 Bunch, J. S. *et al.* Impermeable atomic membranes from graphene sheets. *Nano Lett* **8**, 2458-2462, doi:10.1021/nl801457b (2008).

13 Lee, C., Wei, X., Kysar, J. W. & Hone, J. Measurement of the elastic properties and intrinsic strength of monolayer graphene. *Science* **321**, 385-388, doi:10.1126/science.1157996 (2008).

14 Hencky, H. Uber den Spannungszustand in kreisrunden Platten mit verschwindender Biegungssteifigkeit. *Zeitschrift fur Mathematik und Physik* **63**, 311-317 (1915).

15 Koenig, S. P., Wang, L., Pellegrino, J. & Bunch, J. S. Selective molecular sieving through porous graphene. *Nat Nanotechnol* **7**, 728-732, doi:10.1038/nnano.2012.162 (2012).

16 Drahushuk, L. W., Wang, L., Koenig, S. P., Bunch, J. S. & Strano, M. S. Analysis of Time-Varying, Stochastic Gas Transport through Graphene Membranes. *Acs Nano* **10**, 786-795, doi:10.1021/acsnano.5b05870 (2016).

17 Wang, L. *et al.* Molecular valves for controlling gas phase transport made from discrete angstrom-sized pores in graphene. *Nat Nanotechnol* **10**, 785-790, doi:10.1038/nnano.2015.158 (2015).

18 Sun, P. Z. *et al.* Limits on gas impermeability of graphene. *Nature* **579**, 229-232, doi:10.1038/s41586-020-2070-x (2020).
19 Leterrier, Y. Durability of nanosized oxygen-barrier coatings on polymers. *Progress in Materials Science* **48**, 1-55, doi:https://doi.org/10.1016/S0079-6425(02)00002-6 (2003).
20 Strupinsky, G. & Brody, A. (Proceed San Francisco, CA, 1998).
21 Robeson, L. M. The upper bound revisited. *Journal of Membrane Science* **320**, 390-400, doi:10.1016/j.memsci.2008.04.030 (2008).
22 Xu, K., Cao, P. G. & Heath, J. R. Graphene Visualizes the First Water Adlayers on Mica at Ambient Conditions. *Science* **329**, 1188-1191, doi:10.1126/science.1192907 (2010).
23 Golla, D. *et al.* Optical thickness determination of hexagonal boron nitride flakes. *Appl Phys Lett* **102**, 161906, doi:10.1063/1.4803041 (2013).
24 Northolt, M. G. X-Ray-Diffraction Study of Poly(P-Phenylene Terephthalamide) Fibers. *Eur Polym J* **10**, 799-804, doi:Doi 10.1016/0014-3057(74)90131-1 (1974).
25 Liu, P. *et al.* Layered and scrolled nanocomposites with aligned semi-infinite graphene inclusions at the platelet limit. *Science* **353**, 364-367, doi:10.1126/science.aaf4362 (2016).
26 Kozawa, D. *et al.* Highly Ordered Two-Dimensional MoS2 Archimedean Scroll Bragg Reflectors as Chromatically Adaptive Fibers. *Nano Lett* **20**, 3067-3078, doi:10.1021/acs.nanolett.9b05004 (2020).